A GEOMETRICALLY NONLINEAR COSSERAT SHELL MODEL FOR ORIENTABLE AND NON-ORIENTABLE SURFACES: DISCRETIZATION WITH GEOMETRIC FINITE ELEMENTS

LISA JULIA NEBEL, OLIVER SANDER, MIRCEA BÎRSAN, AND PATRIZIO NEFF

ABSTRACT. We investigate discretizations of a geometrically nonlinear elastic Cosserat shell with nonplanar reference configuration originally introduced by Bîrsan, Ghiba, Martin, and Neff in 2019. The shell model includes curvature terms up to order 5 in the shell thickness, which are crucial to reliably simulate high-curvature deformations such as near-folds or creases. The original model is generalized to shells that are not homeomorphic to a subset of \mathbb{R}^2 . For this, we replace the originally planar parameter domain by an abstract two-dimensional manifold, and verify that the hyperelastic shell energy and three-dimensional reconstruction are invariant under changes of the local coordinate systems. This general approach allows to determine the elastic response for even non-orientable surfaces like the Möbius strip and the Klein bottle. We discretize the model with a geometric finite element method and, using that geometric finite elements are H^1 -conforming, prove that the discrete shell model has a solution. Numerical tests then show the general performance and versatility of the model and discretization method.

Contents

1. Introduction	2
2. Cosserat shell model with general topology	ϵ
2.1. The shell surface and its extrinsic geometry	6
2.2. Kinematics and strain measures	10
2.3. Interpretation and reconstruction	11
2.4. Hyperelastic shell energy functional	14
2.5. Existence of minimizers	18
3. Discretization by geometric finite elements	19
3.1. Discretizing the shell surface	20
3.2. Geometric interpolation rules	21
3.3. Geometric finite element functions	24
4. Discrete and algebraic Cosserat shell problems	25
4.1. The discrete problem	26
4.2. Existence of solutions of the discrete problem	27
4.3. The algebraic problem	31
5. Numerical experiments	32

²⁰¹⁰ Mathematics Subject Classification. Primary: 65N30; Secondary: 74K25.

Key words and phrases. elastic shell, Cosserat model, geometrically nonlinear, nonplanar reference configuration, non-orientable, geometric finite elements, existence, locking.

This research has been funded by the Deutsche Forschungsgemeinschaft (DFG, German Research Foundation) — Project: SA 2130/6-1 (L. Nebel and O. Sander) and Project no. 415894848, NE 902/8-1 (P. Neff) and BI 1965/2-1 (M. Bîrsan).

5.1.	Deflection of a half sphere	32
5.2.	Comparison with alternative models	35
5.3.	Shells with challenging topology	38
5.4.	Buckling of a cylinder under a torsion load	39
5.5.	Non-orientable shell surfaces	41
Refe	erences	43

1. Introduction

In [15, 33], the authors introduced a physically linear but geometrically nonlinear elastic Cosserat shell model for shells with a curved reference configuration. The model was derived by dimensional reduction of a three-dimensional Cosserat continuum model, and it is a direct generalization of the flat Cosserat shell model of Neff [58]. In later papers, different variants of the model were discussed, and justified by derivation [13, 14] or Γ -convergence arguments [65].

Configurations of this Cosserat shell consist of the total deformation $\boldsymbol{m}:\omega\to\mathbb{R}^3$, which maps a two-dimensional parameter domain (the "fictitious domain" in the parlance of [15]) into three-dimensional Euclidean space, and an independent field of microrotations $\boldsymbol{Q}_e:\omega\to\mathrm{SO}(3)$ (where SO(3) is the special orthogonal group, i.e., the group of orthogonal 3×3 matrices with determinant 1), which describes transverse shear and local drilling of the shell. The material behavior is given as a hyperelastic energy functional

$$I(\boldsymbol{m},\boldsymbol{Q}_e) := \int_{\omega} \left[W_{\mathrm{memb}}(\boldsymbol{E}^e,\boldsymbol{K}^e) + W_{\mathrm{bend}}(\boldsymbol{K}^e) \right] d\omega + \text{external loads},$$

which features terms up to order 5 in the shell thickness. The matrix fields E^e and K^e are strain and curvature measures of the shell, depending on the deformation and microrotation, as well as on the geometry of an assumed stress-free reference configuration m_0 . The energy density neatly separates the material coefficients of the original three-dimensional model from geometric properties of the stress-free configuration. The model is geometrically nonlinear but physically linear, which means that it is frame-indifferent and allows for large rotations but only small elastic strains. Nevertheless, existence of minimizers in the space $H^1(\omega, \mathbb{R}^3) \times H^1(\omega, SO(3))$ has been shown [34]. This sets the model apart from other geometrically nonlinear shell models that combine membrane and bending effects, but lack an existence proof. The provable existence of minimizers is an important justification for the use of Cosserat shell models.

In the original shell model in [15, 33] the parameter domain ω was an open set in \mathbb{R}^2 . The model was therefore restricted to shells that are homeomorphic to such sets, which excluded even simple geometries such as spheres. In this paper we reformulate the model for more general topologies. Following ideas from [54], we replace the flat parameter domain ω of [15, 33] by an abstract two-dimensional manifold, again called ω . To address points in this manifold we introduce local coordinate systems, which map open sets of ω homeomorphically to subsets of \mathbb{R}^2 , as is the standard construction in differential geometry. The single flat parameter ("fictitious") domain of [15, 33] is hence replaced by a set of subsets of \mathbb{R}^2 , which serve as local coordinates. The situation of [15, 33] is recovered when the parameter domain ω can be covered by a single coordinate chart.

Configurations of the two-dimensional shell surface are given as immersions m of ω into \mathbb{R}^3 with associated microrotation fields $Q_e:\omega\to \mathrm{SO}(3)$. The immersion $m:\omega\to\mathbb{R}^3$ represents the shape of the shell surface, and the microrotation Q_e is a local rotation of the shell with respect to its configuration in the natural, i.e., stress-free, reference state. This stress-free state is given by a second immersion $m_0:\omega\to\mathbb{R}^3$, which is part of the problem formulation. Unlike in models of non-Euclidean elasticity [12, 27] we explicitly assume the existence of such a stress-free configuration, but note that a large part of this paper would carry over to the more general non-Euclidean case, too.

The approach of using a general manifold ω as the parameter domain may appear unnecessarily abstract at first sight. However, it seems conceptually cleaner to us than using the reference surface $m_0(\omega)$ (a subset of \mathbb{R}^3) for parametrization. Indeed, unlike in the original derivation in [15, 33], the map $m_0(\omega) \to m(\omega)$ (which corresponds to the restriction of the map $\varphi_{\xi}: \Omega_{\xi} \to \Omega_c$ to the two-dimensional set $\omega_{\xi} \subset \Omega_{\xi}$ there) never plays a role. Also, note that we explicitly allow the stress-free configuration $m_0(\omega)$ to have self-intersections, which also makes it unsuitable as a parameter domain. For physically meaningful results, of course, the shell surface may not self-intersect, i.e., the configuration map m has to be an embedding rather than an immersion. However, when investigating non-orientable parameter manifolds ω it turned out that our construction can be effortlessly formulated for the more general case of immersions as well. We therefore write everything in terms of immersions, which then makes the model cover even non-physical but interesting objects like the Klein bottle.

Models of shells with curved reference configurations exist in the literature, but like [15, 33] they never explicitly discuss objects with non-trivial topology [26, 62]. An alternative general shell model able to handle curved reference configurations and complicated topology is the 6-parameter shell. An account of this approach has been presented, e.g., in the book of Libai and Simmonds [53]. Other shell models with curved reference configurations and large rotations are analyzed in the papers [18, 19, 20, 21]. From a kinematical point of view, the 6-parameter shells are equivalent to Cosserat shells, since both models involve the deformation and a microrotation as independent variables. The difference to our approach consists in the constitutive assumptions and the relation to the three-dimensional theory. In contrast to our work, the papers on 6-parameter shells assume the parent three-dimensional model to be a Cauchy continuum (i.e., without microrotations). Also, their assumed constitutive relations are relatively simple, since constitutive coefficients do not depend on the curvature of the reference surface. Further details on geometrically nonlinear shells and their derivation can be found in the monograph [75].

The second part of this manuscript deals with finite element discretizations of the presented Cosserat model. For such discretizations, we equip the shell parameter surface ω with a triangulation, which allows to express all integrals as sums of integrals over a reference triangle. This corresponds to the usual practice when constructing finite element models of curved shells, but is hardly ever spelled out in any detail. Finite element spaces are defined with respect to the triangulation of ω . In particular, we represent configurations of the shell by Lagrange finite element functions $\mathbf{m}_h:\omega\to\mathbb{R}^3$. The given stress-free configuration $\mathbf{m}_0:\omega\to\mathbb{R}^3$ can in principle be represented in any manner, but will most frequently also be represented by a finite element function. While piecewise linear finite elements are possible,

they neutralize some of the advantages of the shell model presented here, because all terms involving the curvature of $m_0(\omega)$ would then vanish. We will therefore mostly use Lagrange finite elements of second order.

The discretization of the microrotation field Q_e requires additional attention. Problems with directional or orientational degrees of freedom such as the field of microrotations $Q_e:\omega\to \mathrm{SO}(3)$ are difficult to treat numerically, because spaces of functions mapping into a nonlinear set such as $\mathrm{SO}(3)$ or the unit sphere S^2 cannot form vector spaces. Consequently, approximations by vector spaces such as spaces of piecewise polynomials are not conforming, in the sense that the image of the approximating map is not contained in $\mathrm{SO}(3)$. Seen from another direction, the problem is that there are no nontrivial $\mathbb{R}^{3\times3}$ -valued polynomials with values in $\mathrm{SO}(3)$. Various ad hoc approaches for discretizations of $\mathrm{SO}(3)$ - or S^2 -valued fields exist in the literature, each with its own strengths and weaknesses. Overviews can be found, e.g., in [52, 55, 64].

To take an example, discretizations based on interpolating Euler angles such as [40, 79] are straightforward to construct, but they are plagued by coordinate singularities near certain configurations, and they are therefore only usable for moderate rotations. Also, the discrete models do not inherit the frame indifference of the continuum model. Similar problems exist for methods that interpolate between values by lifting them onto a fixed tangent space and interpolate there [56, 57, 62]. To avoid large distortions, some methods such as [57] switch between several tangent spaces.

Methods that repeatedly average between pairs of orientations can be interpreted as generalizations of spline functions [1, 4, 43]. They lead to objective and path-independent formulations, but suffer from spurious dependencies of the simulation results on the node ordering. A more difficult approach, originally proposed by Simo and Fox [71, 73], interpolates only the corrections of the Newton method used to solve the shell equilibrium equations. As elements of a tangent space, these corrections can be approximated by piecewise polynomials. For this to work, the values of the nonlinear variables have to be stored as history variables at the quadrature points. The method mixes discretization and solver algorithm, which makes it difficult to analyze. Unfortunately, it also leads to a dependence of the discrete solution on the load path. This was originally shown by Crisfield and Jelenić [22] for the rod model of Simo and Vu-Quoc [72]. In the context of isogeometric analysis, [24, 25] have used a similar approach interpolating with NURBS functions.

One further possibility is the use of nonconforming discretizations. These use standard $\mathbb{R}^{3\times3}$ -valued piecewise polynomials for the approximation of the microrotation field, and enforce the restriction to SO(3) only at the Lagrange points. For Cosserat beams this is mentioned in [11, 64]. For Reissner–Mindlin shells (i.e., shells with only one director), the corresponding technique is used, e.g., in [45] and follow-up work. Such a discretization is simple, singularity-free, and preserves frame indifference. However, the models need to be modified (explicitly or implicitly) to account for the non-orthogonality of the microrotation field away from the Lagrange points. Outside of shell theory, nonconforming discretizations have been analyzed mathematically for maps into the unit sphere S^2 [3, 8]. While the original works considered only first-order finite elements and showed only weak convergence results, quasioptimal convergence could be shown recently for harmonic maps [7] and harmonic map heat

flow [6], even for finite elements of approximation order larger than 1. A numerical study also testing such higher-order discretizations is given in [5].

Recently, geometric finite elements (GFEs) have emerged as an elegant and robust way to discretize the nonlinear vector and orientation fields appearing in geometrically nonlinear director shell models [38, 67, 68, 69]. They are based on generalizations of polynomial interpolation formulas to data in non-Euclidean spaces. Indeed, unlike most previous discretization approaches, GFE methods define actual (nonlinear) spaces of finite element functions. This makes their construction and behavior more transparent, and it allows for rigorous analytical investigations similar to the classical Euclidean finite element theory. Indeed, optimal L^2 and H^1 interpolation error bounds have been shown in [36, 37, 41, 42] for finite element functions of any order, along with discretization error bounds for harmonic maps.

Various ways to generalize polynomial interpolation to manifold-valued data have been proposed in the literature [43]. In this paper we use geodesic [68] and projection-based finite elements [37]. Both allow for approximation functions of arbitrary order, and preserve the frame-indifference of the continuous models. Also, both types of finite element functions are first-order Sobolev functions. This makes analytical investigations much easier than for competing approaches. A case in point for this claim is Chapter 4.2 of this manuscript, where we give a proof for the existence of finite element solutions for the nonlinear shell problem, reusing considerable parts of the existence proof of [34] for the continuous model.

Geometric finite elements have already been used successfully for planar Cosserat shells [70], and for Cosserat rods with initial curvature [67]. Grohs [38] and Müller and Bischoff [55] extended the concept to spline approximation functions, and the latter used it to discretize the 1-director shell model of Simo and Fox [73] (i.e., the geometrically nonlinear Reissner–Mindlin model). Romero [64] lists projecting onto SO(3), i.e., projection-based finite elements, as one way to discretize Cosserat beams. The discretizations have also appeared in experimental studies of the wrinkling behavior of coated substrates [35, 51].

The algebraic formulation of the discrete shell problem is a minimization problem on the product space $\mathbb{R}^{3N_1} \times \mathrm{SO(3)}^{N_2}$ where N_1 and N_2 are the numbers of Lagrange nodes used for discretizing the deformation and microrotation, respectively. This space is a $3N_1+3N_2$ -dimensional Riemannian manifold. We use a Riemannian trustregion algorithm to solve this minimization problem [2]. This is a globalized Newton method replacing each Newton step with a quadratic minimization problem subject to a convex inequality constraint. Standard trust-region methods work only for energies defined on Euclidean spaces, however [2] presents a generalization to energies on Riemannian manifolds. The correction problems of this generalization are quadratic minimization problems on the (linear) tangent spaces of $\mathbb{R}^{3N_1} \times \mathrm{SO(3)}^{N_2}$, again with a convex constraint. To make these large constrained problems feasible, we choose a formulation where the convex constraint consists of separate bound constraints for the individual degrees of freedom. The resulting quadratic minimization problems can then be solved with a monotone multigrid method, as explained in [69]. The challenging computations of the tangent matrices of the energy are done using the automatic differentiation software ADOL-C [77].

When constructing discretizations of shells and plates, locking is always an issue. For objects with a planar stress-free configuration, (shear) locking is determined by the finite elements used for the deformation and the microrotation fields. As it turns

out, if the stress-free geometry is curved, then the approximation of its geometry comes into play as well. Unfortunately, the rigorous understanding and treatment of locking is still out of reach for discretizations of geometrically nonlinear shell models. In this manuscript we therefore only perform numerical tests. We observe that the proposed discretization does not exhibit shear locking if the geometry discretization is at least of second order. This is consistent with, and generalizes, our previous results for shells with a planar stress-free configuration [70].

This article presents the model and the discretization, and shows a set of numerical tests. Chapter 2 presents the generalized shell model. We do not derive it from a three-dimensional model, but we show in detail how it relates to its parent model [15, 33] for simple topologies. Chapter 3 then recalls the geometric finite element method for the approximation of microrotation fields. Chapter 4 presents the discretized shell problem, and proves rigorously that solutions (possibly non-unique) do exist for both geodesic and projection-based finite elements, and for any approximation order.

The article then shows five numerical examples. With the first one, we systematically investigate the model response and locking behavior as they depend on the approximation order for the deformation field, the microrotations, and the reference surface geometry. In a further sequence of tests, we then compare the simulation with an actual three-dimensional shell. We also do a comparison with a variant of the shell model recently proposed by Bîrsan [13]. Further tests show the behavior of shells with a complex topology undergoing large rotations, and for shells that buckle. Finally, to show that the model can properly handle non-orientable shell surfaces, we compute equilibrium configurations of a Möbius strip and a Klein bottle subject to a volume load.

2. Cosserat shell model with general topology

In this first section we introduce the Cosserat shell model. It is a generalization of a model originally derived in [13, 15, 33]. While the original model only allowed for shells that are diffeomorphic to a domain in \mathbb{R}^2 , the new one covers more general topologies.

The original model was introduced twice (in [15] and [33]) using different notations. We mainly follow the tensor notation of [15], but clarify the connection to the matrix notation in [33] when appropriate. Boldface letters are used for vectors and tensors. When Greek letters are used as indices, they always range over the set $\{1,2\}$, and Einstein summation is used.

2.1. The shell surface and its extrinsic geometry. The shell surface is parametrized by an abstract two-dimensional manifold ω , possibly with boundary. If (U, τ) is a coordinate chart, i.e., a homeomorphism from an open set $U \subset \omega$ to a subset of \mathbb{R}^2 , then we write η for a point in ω and $x = \tau(\eta)$ for its local coordinates (Figure 1). The situation of [33] is recovered when ω can be described by a single coordinate patch $U = \omega$, in which case ω can be chosen as a subset of \mathbb{R}^2 , and τ can be the identity map.

Configurations of the shell surface are realized as immersions of ω into \mathbb{R}^3 . Physics require them to be even embeddings, i.e., injective, but we stick to the slightly more general case. The stress-free reference configuration is given as an immersion $\mathbf{m}_0: \omega \to \mathbb{R}^3$. We assume \mathbf{m}_0 to be a map in $H^1(\omega, \mathbb{R}^3)$, with the definition of a

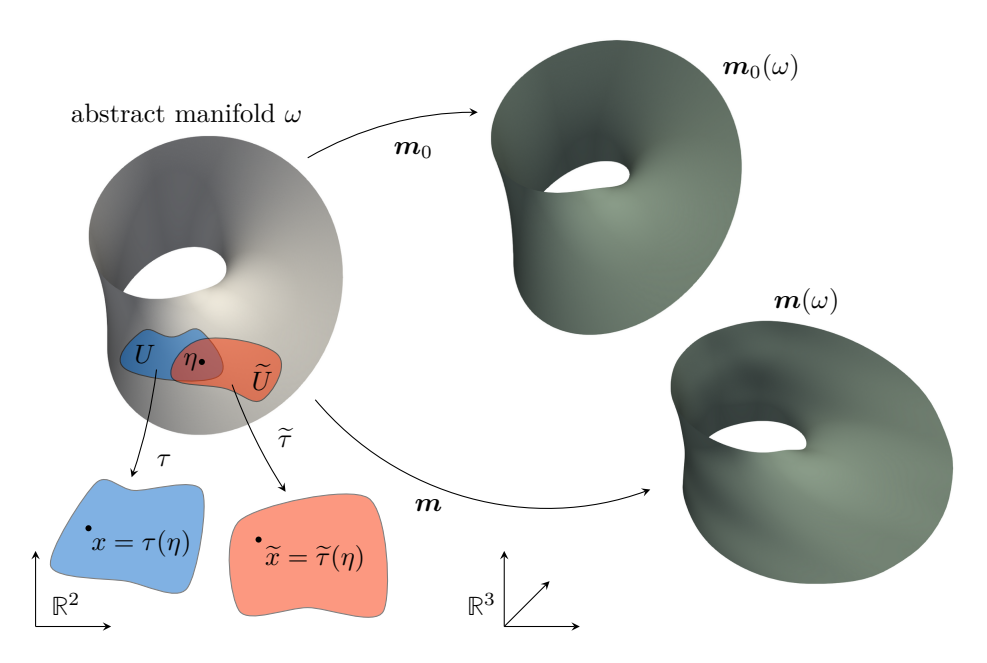


FIGURE 1. Kinematics of the shell surface: The abstract parameter manifold ω is immersed into \mathbb{R}^3 to yield configurations m_0 and m of the shell. Points η on ω are described by local coordinate systems such as $\tau: U \to \mathbb{R}^2$ and $\tilde{\tau}: \tilde{U} \to \mathbb{R}^2$.

Sobolev space on a manifold from [78]. In addition, we require that m_0 is at least piecewise in H^2 , for the second fundamental tensor \boldsymbol{b} to exist almost everywhere. Deformations of the shell surface under load are described by a second immersion $\boldsymbol{m}: \omega \to \mathbb{R}^3$, which we discuss in Section 2.2. For the rest of this section we focus on the initial configuration m_0 . Derivatives appearing below are to be interpreted in the weak sense if appropriate.

The Sobolev smoothness of $m_0: \omega \to \mathbb{R}^3$ allows to define metric and curvature measures of the immersion m_0 in a weak sense.

Definition 1 (Covariant basis vectors). Let η be a point on ω . The covariant basis vectors $\mathbf{a}_1, \mathbf{a}_2 \in \mathbb{R}^3$ at $\eta \in \omega$ are

$$\boldsymbol{a}_1(\eta) := \frac{\partial \boldsymbol{m}_0(\eta)}{\partial x_1}, \qquad \boldsymbol{a}_2(\eta) := \frac{\partial \boldsymbol{m}_0(\eta)}{\partial x_2}.$$

Expressions like these are to be interpreted in local coordinates: If (U, τ) is a coordinate chart with $\eta \in U$, then write $x = \tau(\eta)$ and define

$$\boldsymbol{a}_1(\eta) := \frac{\partial \boldsymbol{m}_0(\tau^{-1}(x))}{\partial x_1}, \qquad \boldsymbol{a}_2(\eta) := \frac{\partial \boldsymbol{m}_0(\tau^{-1}(x))}{\partial x_2}.$$

The map $\mathbf{m}_0 \circ \tau^{-1}$ that appears in these expressions corresponds to what is called $y_0 = \Theta(0)$ in [33].

The covariant basis vectors at η span the tangent space of $\mathbf{m}_0(\omega) \subset \mathbb{R}^3$ at $\mathbf{m}_0(\eta)$. We interpret them as column vectors. In the notation of [33] they represent the first

two columns of

$$\nabla_x \Theta(0) = \left(\frac{\partial}{\partial x_1} \Theta(0) \; \middle| \; \frac{\partial}{\partial x_2} \Theta(0) \; \middle| \; \boldsymbol{n}_0 \right) = (\boldsymbol{a}_1 \; | \; \boldsymbol{a}_2 \; | \; \boldsymbol{n}_0) \in \mathbb{R}^{3 \times 3}.$$

The third column is the unit normal vector field

(1)
$$\boldsymbol{n}_0 \coloneqq \frac{\boldsymbol{a}_1 \times \boldsymbol{a}_2}{\|\boldsymbol{a}_1 \times \boldsymbol{a}_2\|}.$$

The orientation of this field depends on the choice of local coordinates.

We also need the contravariant basis vectors of the tangent spaces of $\mathbf{m}_0(\omega)$. They should be interpreted as row vectors.

Definition 2 (Contravariant basis vectors). At any $\eta \in \omega$, the contravariant basis vectors are the vectors $\mathbf{a}^1(\eta)$, $\mathbf{a}^2(\eta) \in \mathbb{R}^3$ that are orthogonal to $\mathbf{n}_0(\eta)$ and such that $\mathbf{a}_{\alpha}(\eta) \cdot \mathbf{a}^{\beta}(\eta) = \delta_{\alpha\beta}$, where $\delta_{\alpha\beta}$ is the Kronecker delta.

Next, we define the first and second fundamental tensors.

Definition 3 (Fundamental tensors). The first and second fundamental tensors of the immersion $\mathbf{m}_0 : \omega \to \mathbb{R}^3$ are

$$m{a}:\omega o\mathbb{R}^{3 imes 3} \qquad m{a}(\eta)\coloneqq rac{\partial m{m}_0(\eta)}{\partial x_lpha}\otimes m{a}^lpha(\eta)=m{a}_lpha(\eta)\otimes m{a}^lpha(\eta)$$

and

$$m{b}:\omega o\mathbb{R}^{3 imes 3} \qquad m{b}(\eta):=-rac{\partial m{n}_0(\eta)}{\partial x_lpha}\otimes m{a}^lpha(\eta),$$

respectively.

Again, these expressions should be interpreted in local coordinates $x = \tau(\eta)$. Direct computations show that the tensors \boldsymbol{a} and \boldsymbol{b} are symmetric. They are related to the better-known first and second fundamental forms

$$\mathbf{I} := (\nabla \boldsymbol{m}_0)^T \nabla \boldsymbol{m}_0$$
 and $\mathbf{I} := -(\nabla \boldsymbol{m}_0)^T \nabla \boldsymbol{n}_0$

via

$$a = (a^{\alpha} \otimes e_{\alpha}) I(e_{\beta} \otimes a^{\beta})$$

and

$$\boldsymbol{b} = (\boldsymbol{a}^{\alpha} \otimes \boldsymbol{e}_{\alpha}) \mathbb{I}(\boldsymbol{e}_{\beta} \otimes \boldsymbol{a}^{\beta}),$$

where $\nabla m_0 := (a_1|a_2)$ is the 3×2 matrix with columns a_1 and a_2 , and e_1 , e_2 are the canonical basis vectors of \mathbb{R}^2 .

Remark 4. As the quantities a and b are defined with respect to particular coordinate systems, it is important to verify that the definitions are independent of the specific choice. This is indeed the case, but as it turns out, b changes its sign under orientation-reversing coordinate changes. To see both, let η be a point on ω , and let (U,τ) , $(\widetilde{U},\widetilde{\tau})$ be two coordinate charts with $\eta \in U,\widetilde{U}$. Call x and \widetilde{x} the coordinates of η in $\tau(U) \subset \mathbb{R}^2$ and $\widetilde{\tau}(\widetilde{U}) \subset \mathbb{R}^2$, respectively. Then we have the coordinate transformation map $\widetilde{x} \mapsto x$, i.e., $x = (\tau \circ \widetilde{\tau}^{-1})(\widetilde{x})$, defined in an open neighborhood of $\widetilde{\tau}(\eta) \in \mathbb{R}^2$. The Jacobian of this map is

$$G := \begin{pmatrix} \frac{\partial (\tau \circ \widetilde{\tau}^{-1})_1(\widetilde{x})}{\partial \widetilde{x}_1} & \frac{\partial (\tau \circ \widetilde{\tau}^{-1})_1(\widetilde{x})}{\partial \widetilde{x}_2} \\ \frac{\partial (\tau \circ \widetilde{\tau}^{-1})_2(\widetilde{x})}{\partial \widetilde{x}_1} & \frac{\partial (\tau \circ \widetilde{\tau}^{-1})_2(\widetilde{x})}{\partial \widetilde{x}_2} \end{pmatrix}.$$

Suppose that \mathbf{v}_1 , \mathbf{v}_2 are two vector fields that transform like vectors. By this we mean that when we interpret \mathbf{v}_1 , \mathbf{v}_2 to be given locally in coordinates (U, τ) , and $\tilde{\mathbf{v}}_1$, $\tilde{\mathbf{v}}_2$ to be the same vector fields in coordinates $(\tilde{U}, \tilde{\tau})$, then

(2)
$$\widetilde{\boldsymbol{v}}_{\alpha} = \boldsymbol{v}_{\alpha}G, \quad \text{which is} \quad (\widetilde{\boldsymbol{v}}_{1}|\widetilde{\boldsymbol{v}}_{2}) = (\boldsymbol{v}_{1}|\boldsymbol{v}_{2})G.$$

Similarly, let \mathbf{w}^2 , \mathbf{w}^2 be fields that transform like covectors:

$$\begin{pmatrix} \widetilde{\boldsymbol{w}}^1 \\ \widetilde{\boldsymbol{w}}^2 \end{pmatrix} = G^{-1} \begin{pmatrix} \boldsymbol{w}^1 \\ \overline{\boldsymbol{w}}^2 \end{pmatrix}.$$

Then the matrix field $\mathbf{v}_{\alpha} \otimes \mathbf{w}^{\alpha} = \sum_{\alpha=1}^{2} v_{\alpha} w^{\alpha}$ is independent of the coordinates on ω , because

$$\widetilde{m{v}}_{lpha}\otimes\widetilde{m{w}}^{lpha}=\left(\widetilde{m{v}}_{1}|\widetilde{m{v}}_{2}
ight)\left(rac{\widetilde{m{w}}^{1}}{\widetilde{m{w}}^{2}}
ight)=\left(m{v}_{1}|m{v}_{2}
ight)GG^{-1}\left(rac{m{w}^{1}}{m{w}^{2}}
ight)=\left(m{v}_{1}|m{v}_{2}
ight)\left(rac{m{w}^{1}}{m{w}^{2}}
ight)=m{v}_{lpha}\otimesm{w}^{lpha}.$$

The independence of $\mathbf{a} := \mathbf{a}_{\alpha} \otimes \mathbf{a}^{\alpha}$ then follows because $\mathbf{a}_{\alpha} = \partial \mathbf{m}_{0}/\partial x_{\alpha}$ transforms like a vector, and \mathbf{a}^{α} transforms like a covector. Similarly, \mathbf{n}_{0} is invariant under orientation-preserving changes of coordinates, and therefore $\partial \mathbf{n}_{0}/\partial x_{\alpha}$ transforms like a vector, too. This implies that $\mathbf{b} := -\frac{\partial \mathbf{n}_{0}}{\partial x_{\alpha}} \otimes \mathbf{a}^{\alpha}$ is invariant under orientation-preserving coordinate changes. However, if the orientation is reversed, then \mathbf{n}_{0} changes its sign, and so does \mathbf{b} .

The hyperelastic energy of the Cosserat shell model depends on the classical extrinsic curvature measures (Gauß curvature and mean curvature) of the immersed shell surface $m_0(\omega)$. These can be computed conveniently from the second fundamental tensor:

Lemma 5 (Curvature [15, Section 3.1]). Let κ_1 and κ_2 be the principal curvatures of $\mathbf{m}_0(\omega)$, wherever defined. Then the Gauss curvature $K := \kappa_1 \cdot \kappa_2$ and the mean curvature $H := \frac{1}{2}(\kappa_1 + \kappa_2)$ can be expressed as

$$K = \det(\boldsymbol{b}), \qquad H = \frac{1}{2}\operatorname{tr}(\boldsymbol{b}).$$

Note that K is independent of the orientation, but H is not.

Finally, the hyperelastic energy involves the alternating pseudo-tensor of the immersed surface.

Definition 6 (Surface alternating pseudo-tensor). The alternating pseudo-tensor of the immersed surface $m_0(\omega)$ is

$$egin{aligned} oldsymbol{c} : \omega &
ightarrow \mathbb{R}^{3 imes 3}, \qquad oldsymbol{c} := rac{1}{\sqrt{\det\left((
abla m_0)^T
abla m_0
ight)}} ig(oldsymbol{a}_1 \otimes oldsymbol{a}_2 - oldsymbol{a}_2 \otimes oldsymbol{a}_1ig) \ &= \sqrt{\det\left((
abla m_0)^T
abla m_0ig)} ig(oldsymbol{a}^1 \otimes oldsymbol{a}^2 - oldsymbol{a}^2 \otimes oldsymbol{a}^1ig). \end{aligned}$$

Direct computation shows that the matrix c is skew-symmetric, and that it is indeed a pseudo-tensor, because, if \tilde{c} is a representation with respect to a second

coordinate chart,

$$\widetilde{\boldsymbol{c}} = \frac{1}{\sqrt{\det\left((\nabla \widetilde{\boldsymbol{m}}_0)^T \nabla \widetilde{\boldsymbol{m}}_0\right)}} (\widetilde{\boldsymbol{a}}_1 \otimes \widetilde{\boldsymbol{a}}_2 - \widetilde{\boldsymbol{a}}_2 \otimes \widetilde{\boldsymbol{a}}_1)$$

$$= \frac{\det G}{\sqrt{(\det G)^2 \det\left((\nabla \boldsymbol{m}_0)^T \nabla \boldsymbol{m}_0\right)}} (\boldsymbol{a}_1 \otimes \boldsymbol{a}_2 - \boldsymbol{a}_2 \otimes \boldsymbol{a}_1)$$

$$= \operatorname{sgn}(\det G) \cdot \boldsymbol{c}.$$

Also, it is a linear complex structure on each tangent space, because $c^2 = -a$ and a is the identity on the tangent space.

Remark 7 (Relationship to [33]). In the language of [33, Section 3.2], the tensors a, b, and c are defined in terms of the map

$$\nabla_x \Theta(0) = (\nabla y_0 \mid n_0),$$

and read

$$\begin{split} A_{y_0} &:= (\nabla y_0 | 0) [\nabla_x \Theta(0)]^{-1} \\ B_{y_0} &:= -(\nabla n_0 | 0) [\nabla_x \Theta(0)]^{-1} \\ C_{y_0} &:= \det(\nabla_x \Theta(0)) [\nabla_x \Theta(0)]^{-T} \begin{pmatrix} 0 & 1 & 0 \\ -1 & 0 & 0 \\ 0 & 0 & 0 \end{pmatrix} [\nabla_x \Theta(0)]^{-1}. \end{split}$$

Since

$$\nabla_x \Theta(0) = (\nabla y_0 | n_0) = (\boldsymbol{a}_1 | \boldsymbol{a}_2 | \boldsymbol{n}_0) \quad and \quad [\nabla_x \Theta(0)]^{-1} = \begin{pmatrix} \boldsymbol{a}_1^1 \\ \boldsymbol{a}_2^2 \\ \boldsymbol{n}_0 \end{pmatrix}$$

in our notation, we do get $\mathbf{a} = A_{y_0}$, $\mathbf{b} = B_{y_0}$, and $\mathbf{c} = C_{y_0}$.

2.2. Kinematics and strain measures. In Cosserat theory, the configuration of a shell is given by a deformation of the shell surface together with an independent field of rotations, called the *microrotation field*. The shell surface deformation is described by a function $\boldsymbol{m}:\omega\to\mathbb{R}^3$. Physical models would require injectivity of \boldsymbol{m} , but we explicitly allow \boldsymbol{m} to be non-injective, and therewith accommodate objects like the Klein bottle of Chapter 5.5. The microrotation field $\boldsymbol{Q}_e:\omega\to\mathrm{SO}(3)$ models rotations of infinitesimal parts of the shell (see Chapter 2.3 below for details on the interpretation). In the reference configuration, \boldsymbol{Q}_e will be the identity matrix field.

At any point $\eta \in \omega$ around which $\mathbf{m}_0(\omega)$ is sufficiently smooth we define strain measures for the shell surface deformation and the microrotation field. The geometry of the shell surface $\mathbf{m}_0(\omega)$ enters these expressions in form of the metric tensor $\mathbf{a}: \omega \to \mathbb{R}^{3\times 3}$ of Chapter 2.1.

Definition 8 (Strain tensors). The shell strain tensor is

$$m{E}^e:\omega o\mathbb{R}^{3 imes 3} \qquad m{E}^e(\eta):=m{Q}_e^T(\eta)rac{\partial m{m}(\eta)}{\partial x_lpha}\otimes m{a}^lpha(\eta)-m{a}(\eta),$$

and the shell bending-curvature tensor is

$$\boldsymbol{K}^e: \omega \to \mathbb{R}^{3\times 3} \qquad \boldsymbol{K}^e(\eta) := \operatorname{axl}\left(\boldsymbol{Q}_e^T(\eta) \frac{\partial \boldsymbol{Q}_e(\eta)}{\partial x_\alpha}\right) \otimes \boldsymbol{a}^\alpha(\eta).$$

Here, the map $axl(\cdot): \mathfrak{so}(3) \to \mathbb{R}^3$ computes the axial vector of a given skew-symmetric 3×3 matrix

$$axl(A) := (A_{23}, A_{31}, A_{12})^T \in \mathbb{R}^3$$
 with $A = (A_{ij}) \in \mathbb{R}^{3 \times 3}$.

The matrix $\mathbf{Q}_e^T \frac{\partial \mathbf{Q}_e}{\partial x_\alpha}$ really is skew symmetric, because $\frac{\partial (\mathbf{Q}^T \mathbf{Q})}{\partial x_\alpha} = 0$ for any field of orthogonal matrices \mathbf{Q} . The partial derivatives in the expressions for \mathbf{E}^e and \mathbf{K}^e are to be interpreted with respect to an arbitrary coordinate chart (U, τ) around η . The image $\tau(U) \subset \mathbb{R}^2$ of this chart then corresponds to the flat "fictitious" domain ω of [33]. Indeed, in view of equation (4.36) of [33], the quantities \mathbf{E}^e and \mathbf{K}^e correspond to the strains

$$\mathcal{E}_{m,s} := \overline{Q}_{e,s}^T \left(\nabla m \mid \overline{Q}_{e,s} \nabla_x \Theta(0) e_3 \right) \left[\nabla_x \Theta(0) \right]^{-1} - \mathbb{1}_3$$

$$\mathcal{K}_{e,s} := \left(\operatorname{axl} \left(\overline{Q}_{e,s}^T \partial_{x_1} \overline{Q}_{e,s} \right) \mid \operatorname{axl} \left(\overline{Q}_{e,s}^T \partial_{x_2} \overline{Q}_{e,s} \right) \mid 0 \right) \left[\nabla_x \Theta(0) \right]^{-1}$$

defined there. In these expressions, $\Theta(0)$ corresponds to $\mathbf{m}_0 \circ \tau^{-1}$, and its inverse Jacobian is $\left[\nabla_x \Theta(0)\right]^{-1} = \begin{pmatrix} \frac{\mathbf{a}^1}{\mathbf{a}^2} \\ \frac{\mathbf{a}^2}{\mathbf{n}_0} \end{pmatrix}$. The tensor $\overline{Q}_{e,s}$ (defined in equation (4.2) of [33]) corresponds to our \mathbf{Q}_e .

Remark 9. Note that the quantities \mathbf{E}^e and \mathbf{K}^e are independent of the coordinates on ω . Continuing the reasoning of Remark 4, $\mathbf{Q}_e^T \frac{\partial \mathbf{m}}{\partial x_{\alpha}}$ transforms like a vector, and therefore

$$oldsymbol{E}^e = \left(oldsymbol{Q}_e^T rac{\partial oldsymbol{m}}{\partial x_lpha} - rac{\partial oldsymbol{m}_0}{\partial x_lpha}
ight) \otimes oldsymbol{a}^lpha$$

is independent of the coordinates. To show that $\mathbf{K}^e := \operatorname{axl}\left(\mathbf{Q}_e^T \frac{\partial \mathbf{Q}_e}{\partial x_\alpha}\right) \otimes \mathbf{a}^\alpha$ is coordinate-independent, it is sufficient to show that $\operatorname{axl}\left(\mathbf{Q}_e^T \frac{\partial \mathbf{Q}_e}{\partial x_\alpha}\right)$ transforms like a vector, i.e., that

$$\left(\operatorname{axl}\left(\widetilde{\boldsymbol{Q}_{e}}^{T}\frac{\partial\widetilde{\boldsymbol{Q}_{e}}}{\partial x_{1}}\right)\middle|\operatorname{axl}\left(\widetilde{\boldsymbol{Q}_{e}}^{T}\frac{\partial\widetilde{\boldsymbol{Q}_{e}}}{\partial x_{2}}\right)\right) = \left(\operatorname{axl}\left(\boldsymbol{Q}_{e}^{T}\frac{\partial\boldsymbol{Q}_{e}}{\partial x_{1}}\right)\middle|\operatorname{axl}\left(\boldsymbol{Q}_{e}^{T}\frac{\partial\boldsymbol{Q}_{e}}{\partial x_{2}}\right)\right)G.$$

This follows by direct computation.

2.3. Interpretation and reconstruction. The constructions of the two previous sections have been shown to be invariant under orientation-preserving coordinate changes. However, some quantities like the normal vector n_0 and the second fundamental tensor b change their signs under changes of coordinates that switch the orientation. To show that the model is suitable nevertheless to represent actual thin elastic objects we have to show that the model is independent of the choice of orientation. By this we mean that the three-dimensional reconstruction that can be obtained from the shell model is independent of the choice of coordinates and orientation. As a by-product we obtain the result that the shell model is meaningful even for non-orientable parameter surfaces ω .

We start with a discussion of the meaning of the microrotation field Q_e . This field is typically interpreted as a transversal shear and local drilling of the shell. More formally, we equip the initial reference surface $m_0(\omega)$ with an initial microrotation field Q_0 that captures its local orientation.

Definition 10 (Reference microrotation). The reference microrotation of $\mathbf{m}_0(\omega)$ is given by the orthogonal part of the polar decomposition of the matrix $(\nabla \mathbf{m}_0 \mid \mathbf{n}_0) \in \mathbb{R}^{3\times 3}$

$$Q_0 := \operatorname{polar}(\nabla m_0 \mid n_0).$$

In a sense, the orientation Q_0 obtained by this is the closest orthogonal approximation to the deformation gradient $(\nabla \boldsymbol{m}_0 \mid \boldsymbol{n}_0)$ [30]. The columns \boldsymbol{d}_1^0 , \boldsymbol{d}_2^0 , \boldsymbol{d}_3^0 of \boldsymbol{Q}_0 are called directors, and they form an orthonormal frame. By the particular construction of $(\nabla \boldsymbol{m}_0 \mid \boldsymbol{n}_0)$ we further know that $\det(\nabla \boldsymbol{m}_0 \mid \boldsymbol{n}_0) > 0$, and hence $\det \boldsymbol{Q}_0 = 1$, i.e., $\boldsymbol{Q}_0 \in \mathrm{SO}(3)$ everywhere. Similar local frames appear in many other shell models, e.g., [10, 45, 62].

Even though Q_0 is presented in Definition 10 as a quantity defined on all of ω , it is actually local: Both terms ∇m_0 and n_0 imply the choice of a local coordinate system, and $Q_0 := \operatorname{polar}(\nabla m_0 \mid n_0)$ does depend on this choice. This is not an issue in [33], where the model is represented with respect to one single fixed coordinate system only. However, from the more general viewpoint considered here we have to conclude that Q_0 has no independent physical meaning. It only serves to allow an interpretation of Q_e as a change of the local orientation. An exception is the transverse director d_3^0 , for which it is shown in [15, Chapter 3.2] that

$$d_3^0 = n_0.$$

Furthermore, since the reference surface $\mathbf{m}_0: \omega \to \mathbb{R}^3$ is only required to be in H^1 and piecewise in H^2 , it may, for example, have kinks, across which the deformation gradient $\nabla \mathbf{m}_0$ and normal \mathbf{n}_0 are discontinuous. Consequently, \mathbf{Q}_0 also cannot be expected to be continuous even in a single coordinate chart. As it turns out, though, \mathbf{Q}_0 does not appear in the reconstruction formula or in any of the proofs of existence of solutions. Sign flips of \mathbf{n}_0 on non-orientable surfaces ω will be accounted for in the reconstruction formula below.

The microrotation under load Q_e is instead interpreted as acting on the initial microrotation field Q_0 , to yield the total microrotation $\overline{R} := Q_e Q_0$. Unlike m, therefore, Q_e is a relative quantity. Of particular interest is the rotated transverse director

$$d_3 := Q_e d_3^0 = Q_e n_0,$$

which appears in the reconstruction formula below. Note that d_3 is not necessarily orthogonal to the deformed shell surface $m(\omega)$ anymore. Also, like Q_0 , the total microrotation \overline{R} is not usually continuous. This does not pose any problem, because only the three-dimensional reconstruction is of physical relevance.

We now show how a three-dimensional thin shell can be reconstructed from a configuration of the Cosserat shell model. The construction generalizes the approach of [33] to general parameter domains ω . Locally, for a fixed arbitrary coordinate chart, the construction of [33] is recovered. This justifies our model even though we have not directly derived it from a three-dimensional model. Presumably such a derivation is possible if $m_0(\omega)$ is an embedding, and it would follow the steps in [15, 33] locally in coordinate charts.

In [15, 33] the two-dimensional flat parameter domain ω is extended by Cartesian multiplication to a thin three-dimensional parameter domain $\Omega_h := \omega \times (-\frac{h}{2}, \frac{h}{2})$. To generalize this to the case of the abstract two-dimensional parameter surfaces ω

¹It does appear in the existence proof in [34], but on close inspection that proof turns out to be independent of Q_0 . See Section 4.2.

considered here, the corresponding three-dimensional domain is a tubular neighborhood of ω : Let $(\mathcal{N}, \pi, \omega)$ be the normal bundle over ω with respect to the immersion m_0 [23]. It is a three-dimensional vector bundle, and it is orientable as a three-dimensional manifold.² Its fibres are isomorphic to the one-dimensional vector space \mathbb{R} , and we construct it such that the structure group is $O(1) = \{-1, 1\}$. Define a subbundle $(\mathcal{N}_h, \pi, \omega)$ such that the fiber $\pi^{-1}(\eta)$ over each point $\eta \in \omega$ is an open set that contains 0. Local trivializations can then be chosen to take the form $\tau(U) \times \left(-\frac{h}{2}, \frac{h}{2}\right)$, where (τ, U) is a coordinate chart of ω and hence $\tau(U)$ is an open set in \mathbb{R}^2 . These local trivializations correspond to the single set Ω_h employed in [15, 33].

The reconstruction of a three-dimensional deformed configuration from a twodimensional Cosserat shell is a map $\varphi_s : \mathcal{N}_h \to \mathbb{R}^3$, the immersion of a threedimensional object into \mathbb{R}^3 . In coordinates, the reconstruction has the form

(3)
$$\varphi_s: \tau(U) \times (-\frac{h}{2}, \frac{h}{2}) \to \mathbb{R}^3$$

$$\varphi_s(x_1, x_2, x_3) := \mathbf{m}(x_1, x_2) + x_3 \rho_m(x_1, x_2) \mathbf{d}_3(x_1, x_2) + \frac{1}{2} x_3^2 \rho_b(x_1, x_2) \mathbf{d}_3(x_1, x_2),$$

which is the formula from [15, 33], but is now interpreted as an expression of local coordinates $x = (x_1, x_2) \in \tau(U)$ of a point $\eta \in \omega$. (In an abuse of notation we have omitted various occurrences of τ^{-1} here.) Additionally, x_3 is the coordinate of the interval $(-\frac{h}{2}, \frac{h}{2})$. The coefficient functions are

$$\rho_m := 1 - \frac{\lambda}{\lambda + 2\mu} (\operatorname{tr} \boldsymbol{E}^e)$$

and

$$\rho_b := -\frac{\lambda}{\lambda + 2\mu} (\operatorname{tr}(\boldsymbol{E}^e \boldsymbol{b} + c \boldsymbol{K}^e)),$$

where λ and μ are the Lamé parameters.

Lemma 11. The reconstruction (3) is independent of the coordinates on ω . It is well-defined even if ω is not orientable.

Proof. By Remarks 4 and 9, the scalar-valued coefficient functions $\rho_m: \tau(U) \to \mathbb{R}$ and $\rho_b: \tau(U) \to \mathbb{R}$ are independent of the choice of coordinates on ω ; only ρ_b flips its sign under orientation-reversing coordinate changes. To see the independence of φ_s , let U and \widetilde{U} be two overlapping coordinate charts of ω . We call the corresponding local coordinates $x=(x_1,x_2)$ and $\widetilde{x}=(\widetilde{x}_1,\widetilde{x}_2)$, respectively, and extend them to coordinates (x_1,x_2,x_3) and $(\widetilde{x}_1,\widetilde{x}_2,\widetilde{x}_3)$ of the corresponding locals trivializations $\tau(U)\times(-\frac{h}{2},\frac{h}{2})$ and $\widetilde{\tau}(\widetilde{U})\times(-\frac{h}{2},\frac{h}{2})$, respectively, of the normal bundle $(\mathcal{N}_h,\pi,\omega)$. As the normal bundle is orientable as a manifold, we only need to consider orientation-preserving coordinate changes $(\widetilde{x}_1,\widetilde{x}_2,\widetilde{x}_3)\mapsto(x_1,x_2,x_3)$. Since these are coordinate changes of a (truncated) rank-1 vector bundle we can look at transformations $(x_1,x_2)\mapsto(\widetilde{x}_1,\widetilde{x}_2)$ and $x_3\mapsto\widetilde{x}_3$ separately, and since we have used O(1) as the structure group the only possible transformations for the latter are $\widetilde{x}_3=x_3$ and $\widetilde{x}_3=-x_3$. Regarding the overall orientation, we therefore have to distinguish only two cases:

- (1) $(\widetilde{x}_1, \widetilde{x}_2) \mapsto (x_1, x_2)$ preserves orientation. Then $\widetilde{x}_3 = x_3$.
- (2) $(\widetilde{x}_1, \widetilde{x}_2) \mapsto (x_1, x_2)$ inverts orientation. Then \widetilde{x}_3 must equal $-x_3$ to make $(x_1, x_2, x_3) \mapsto (\widetilde{x}_1, \widetilde{x}_2, \widetilde{x}_3)$ orientation-preserving again.

 $^{^2}$ Thanks to Andreas Thom (Technische Universität Dresden) for this result.

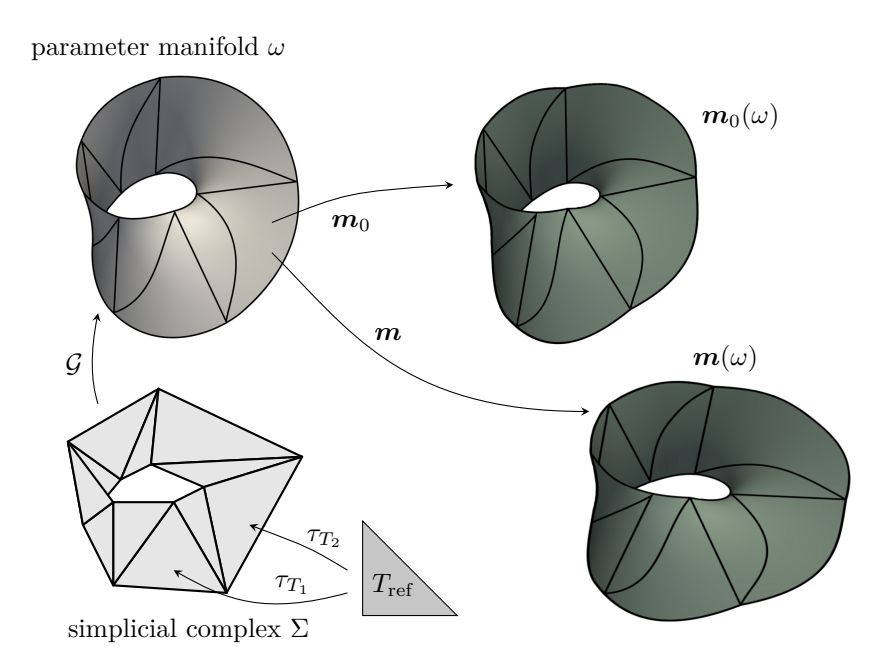


FIGURE 2. Triangulation of the abstract parameter manifold ω , its triangulation by a simplicial complex Σ , and its immersions into \mathbb{R}^3

In the first case, d_3 is invariant under the change of coordinates, and so is the entire reconstruction formula φ_s . In the second case, d_3 changes its sign. However, so does x_3 , and the middle addend of (3) remains invariant. To see invariance of the last term note that x_3^2 does not change sign but ρ_b does, and therefore the sign change of d_3 is compensated for again.

The reconstruction is continuous only if $m:\omega\to\mathbb{R}^3$ is continuously differentiable, because otherwise d_3 may be discontinuous.

Remark 12. The reconstruction formula (3) given here corresponds to the shell energy functional presented in the following chapter. For the variant of that energy discussed in Remark 17, a slightly different reconstruction formula has to be used. The details are given in [13].

2.4. **Hyperelastic shell energy functional.** We assume that the shell behavior can be described by a hyperelastic material. For the case of a single coordinate patch, the authors of [15] and [33] derived an energy functional of the form

$$I(\boldsymbol{m}, \boldsymbol{Q}_e) := \int_{\omega} \left[W_{\mathrm{memb}}(\boldsymbol{E}^e, \boldsymbol{K}^e) + W_{\mathrm{bend}}(\boldsymbol{K}^e) \right] d\omega - \Pi_{\mathrm{ext}}(\boldsymbol{m}, \boldsymbol{Q}_e)$$

by dimensional reduction of a three-dimensional Cosserat material. While in these works the parameter domain ω was a flat domain in \mathbb{R}^2 , it is now an abstract two-dimensional manifold. To integrate the energy density over this manifold, we eschew the traditional approach using a partition of unity on ω . Rather, anticipating the numerical approximation of shell problems by the finite element method, we cover ω by a triangulation. In the following definition, Σ is a pure two-dimensional

simplicial complex. By $|\Sigma|$ we denote the polyhedron of Σ , i.e., the union of all of its simplices.

Definition 13 (Triangulation [76]). A triangulation of ω is a simplicial complex Σ , together with a homeomorphism $\mathcal{G}: |\Sigma| \to \omega$. We call \mathcal{T} the set of triangles of ω , i.e., the set of the images of the two-dimensional simplices of Σ under the map $|\Sigma| \to \omega$.

For each two-dimensional simplex S of Σ , there is an affine homeomorphism from a fixed open triangle $T_{\rm ref} \subset \mathbb{R}^2$ to S, unique up to permutations of the triangle vertices. In finite element parlance, $T_{\rm ref}$ is the reference triangle. Concatenating this homeomorphism with the triangulation map \mathcal{G} we obtain maps $\tau_T : T_{\rm ref} \to T \subset \omega$ for each triangle T in \mathcal{T} (Figure 2). In the following we will only use the maps τ_T , $T \in \mathcal{T}$, and not the simplicial complex Σ . The reason we nevertheless have to introduce Σ for the definition of our triangulation is to make sure that the local coordinates induced by the maps τ_T on the triangles match at the triangle edges. Later, the triangles will form the finite element grid.

To compute integrals over ω , we further need an area element. We use the one induced by the reference immersion which, in local coordinates $\tau: \eta \mapsto x$, reads

(4)
$$d\omega := \sqrt{\det\left((\nabla \boldsymbol{m}_0)^T \nabla \boldsymbol{m}_0\right)} \, dx_1 \, dx_2.$$

We then split the integral along the triangulation \mathcal{T} , and we rewrite the energy as a sum over the triangles

$$I(\boldsymbol{m}, \boldsymbol{Q}_e) = \sum_{T \in \mathcal{T}} \int_T \left[W_{\text{memb}}(\boldsymbol{E}^e, \boldsymbol{K}^e) + W_{\text{bend}}(\boldsymbol{K}^e) \right] \sqrt{\det((\nabla \boldsymbol{m}_0)^T \nabla \boldsymbol{m}_0)} \, dx_1 \, dx_2 - \Pi_{\text{ext}}(\boldsymbol{m}, \boldsymbol{Q}_e).$$

The energy density in (5) depends on the pair (m, Q_e) through the strain measures E^e and K^e . It consists of a membrane part

(6)
$$W_{\text{memb}}(\boldsymbol{E}^e, \boldsymbol{K}^e) := \left(h - K\frac{h^3}{12}\right)W_{\text{m}}(\boldsymbol{E}^e) + \left(\frac{h^3}{12} - K\frac{h^5}{80}\right)W_{\text{m}}(\boldsymbol{E}^e\boldsymbol{b} + c\boldsymbol{K}^e) + \frac{h^3}{6}W_{\text{mixt}}(\boldsymbol{E}^e, c\boldsymbol{K}^e\boldsymbol{b} - 2Hc\boldsymbol{K}^e) + \frac{h^5}{80}W_{\text{mp}}\left((\boldsymbol{E}^e\boldsymbol{b} + c\boldsymbol{K}^e)\boldsymbol{b}\right),$$

and a bending-curvature part

$$W_{\mathrm{bend}}(\boldsymbol{K}^e) := \left(h - K\frac{h^3}{12}\right) W_{\mathrm{curv}}(\boldsymbol{K}^e) + \left(\frac{h^3}{12} - K\frac{h^5}{80}\right) W_{\mathrm{curv}}(\boldsymbol{K}^e \boldsymbol{b}) + \frac{h^5}{80} W_{\mathrm{curv}}(\boldsymbol{K}^e \boldsymbol{b}^2).$$

The parameter h > 0 represents the thickness of the shell. The values K and H are the Gauss and mean curvatures of $m_0(\omega)$, respectively, and a, b, and c are the fundamental tensors and the alternating pseudo-tensor of the reference shell surface $m_0(\omega)$ from Definitions 3 and 6, respectively. All these quantities are defined on the abstract parameter surface ω , and can be expressed in flat coordinates by means of local coordinate charts.

Remark 14. Note that some of the terms in (6) and (7) involve the quantities \mathbf{b}, \mathbf{c} , and H, which depend on the orientation of the surface. However, these quantities always either appear in pairs such that the orientation-dependence cancels, or they

appear as arguments of quadratic functionals (see below), and therefore the sign does not matter. Consequently, the integral (5) is independent of the choice of orientation, and it is well defined even for non-orientable surfaces.

Of the functionals appearing in (6) and (7), W_{mixt} is a bilinear form on $\mathbb{R}^{3\times3} \times \mathbb{R}^{3\times3}$ and W_{m} , W_{mp} , and W_{curv} are quadratic forms on $\mathbb{R}^{3\times3}$. For their explicit representations define

$$\operatorname{sym} X := \frac{1}{2} (X + X^T), \quad \operatorname{skew} X := \frac{1}{2} (X - X^T), \quad \operatorname{dev}_3 X := X - \frac{1}{3} (\operatorname{tr} X) \mathbb{1}_3.$$

$$W_{\text{mixt}}(X,Y) := \mu \langle \operatorname{sym} X, \operatorname{sym} Y \rangle + \mu_c \langle \operatorname{skew} X, \operatorname{skew} Y \rangle + \frac{\lambda \mu}{\lambda + 2\mu} (\operatorname{tr} X) \cdot (\operatorname{tr} Y)$$

$$W_{\text{m}}(X) := \mu \|\operatorname{sym} X\|^2 + \mu_c \|\operatorname{skew} X\|^2 + \frac{\lambda \mu}{\lambda + 2\mu} (\operatorname{tr} X)^2$$

$$W_{\text{mp}}(X) := \mu \|\operatorname{sym} X\|^2 + \mu_c \|\operatorname{skew} X\|^2 + \frac{\lambda}{2} (\operatorname{tr} X)^2$$

(8)
$$W_{\text{curv}}(X) := \mu L_c^2 \Big(b_1 \|\text{dev}_3 \operatorname{sym} X\|^2 + b_2 \|\text{skew } X\|^2 + b_3 (\operatorname{tr} X)^2 \Big).$$

The parameters μ and λ are the Lamé constants of classical elasticity. The coefficient $L_c>0$ is an internal length scale, $b_1,b_2,b_3>0$ are curvature coefficients, and $\mu_c\geq 0$ is the Cosserat couple modulus. Keeping in mind that the bending–curvature tensor \boldsymbol{K}^e has the dimension of inverse length L^{-1} and the curvatures \boldsymbol{b} and K have dimension of inverse length squared L^{-2} , the dimension of L_c is indeed a length L , and the b_1,b_2,b_3 are dimensionless. Note further that $W_{\mathrm{m}}(X)=W_{\mathrm{mixt}}(X,X)$ and $W_{\mathrm{mp}}(X)=W_{\mathrm{m}}(X)+\frac{\lambda^2}{2(\lambda+2\mu)}(\mathrm{tr}\,X)^2$.

Lemma 15. The energy functional I defined in (5) (without the external load potential Π_{ext}) is frame-indifferent in the sense that

(9)
$$I(\mathbf{R}\mathbf{m}, \mathbf{R}\mathbf{Q}_e) = I(\mathbf{m}, \mathbf{Q}_e)$$

for all constant rotations $\mathbf{R} \in SO(3)$.

Remark 16. If the reference configuration $m_0(\omega)$ is a subset of $(x_1, x_2, 0) \subset \mathbb{R}^3$, then the shell surface curvature measures K, H, \mathbf{b} vanish and the model reduces to the Cosserat flat shell model of [58, 70], but with a modified curvature tensor. See [33, Section 5.2] for a discussion.

The term Π_{ext} in (5) represents external loads acting on the shell. We focus here on loads acting on the deformation, and disregard possible orientation loads. Let $\gamma_t \subset \partial \omega$ be a subset of the shell surface boundary. We assume that the load on γ_t can be expressed via a density function $\mathbf{t} \in L^2(\gamma_t, \mathbb{R}^3)$. Analogously, we assume that the load on the body ω can be expressed via a function $\mathbf{f} \in L^2(\omega, \mathbb{R}^3)$. Then we define the potential of the two loads resulting from \mathbf{f} and \mathbf{t} as

(10)
$$\Pi_{\text{ext}}(\boldsymbol{m}, \boldsymbol{Q}_e) := \int_{\gamma_t} \langle \boldsymbol{t}, \boldsymbol{m} - \boldsymbol{m}_0 \rangle \, ds + \int_{\omega} \langle \boldsymbol{f}, \boldsymbol{m} - \boldsymbol{m}_0 \rangle \, d\omega.$$

This corresponds to the term used in [34], without the loads for the microrotations.

Remark 17. Following a slightly more general ansatz, Bîrsan [13] derived the following closely related shell energy density

$$W_{\text{shell, alt}}(\boldsymbol{E}^e, \boldsymbol{K}^e) := W_{\text{memb, alt}}(\boldsymbol{E}^e, \boldsymbol{K}^e) + W_{\text{curv}}(\boldsymbol{K}^e),$$

with the same density for the bending-curvature part (7), but with an alternative membrane density

$$W_{\text{memb, alt}}(\boldsymbol{E}^{e}, \boldsymbol{K}^{e}) := \left(h - K\frac{h^{3}}{12}\right) W_{\text{Coss}}(\boldsymbol{E}^{e}) + \left(\frac{h^{3}}{12} - K\frac{h^{5}}{80}\right) W_{\text{Coss}}(\boldsymbol{E}^{e}\boldsymbol{b} + \boldsymbol{c}\boldsymbol{K}^{e})$$

$$+ \frac{h^{3}}{6} W_{\text{Coss}}(\boldsymbol{E}^{e}, \boldsymbol{c}\boldsymbol{K}^{e}\boldsymbol{b} - 2H\boldsymbol{c}\boldsymbol{K}^{e}) + \frac{h^{5}}{80} W_{\text{Coss}}((\boldsymbol{E}^{e}\boldsymbol{b} + \boldsymbol{c}\boldsymbol{K}^{e})\boldsymbol{b}).$$

The density $W_{\rm memb, alt}(\boldsymbol{E}^e, \boldsymbol{K}^e)$ looks formally like $W_{\rm memb}(\boldsymbol{E}^e, \boldsymbol{K}^e)$ from Equation (6); however, the bilinear and quadratic forms $W_{\rm m}$, $W_{\rm mixt}$ and $W_{\rm mp}$ are all replaced by

$$\begin{split} W_{\text{Coss}}(X,Y) &:= W_{\text{mixt}}(X,Y) - \frac{(\mu - \mu_c)^2}{2(\mu + \mu_c)} (\boldsymbol{n}_0 X) \cdot (\boldsymbol{n}_0 Y) \\ &= \mu \langle \operatorname{sym} X, \operatorname{sym} Y \rangle + \mu_c \langle \operatorname{skew} X, \operatorname{skew} Y \rangle \\ &+ \frac{\lambda \mu}{\lambda + 2\mu} (\operatorname{tr} X) \cdot (\operatorname{tr} Y) - \frac{(\mu - \mu_c)^2}{2(\mu + \mu_c)} (\boldsymbol{n}_0 X) \cdot (\boldsymbol{n}_0 Y) \end{split}$$

or

$$W_{\text{Coss}}(X) := W_{\text{Coss}}(X, X).$$

To see that the difference to (6) is smaller than it seems, note that the tensors E^e , K^e , and b are all of the form

(12)
$$X = \sum_{\substack{i=1,2,3\\\alpha=1,2}} X^i{}_{\alpha} \boldsymbol{a}_i \otimes \boldsymbol{a}^{\alpha} \qquad (with \ \boldsymbol{a}_3 := \boldsymbol{n}_0),$$

i.e., their kernels always contain n_0 (Note that α ranges form 1 to 2, but that i ranges from 1 to 3). As a consequence, all arguments of W_{Coss} in (11) and of W_{memb} in (6) are also of this form. For such tensors X, Y we get, with the split

$$X = \mathbb{1}_3 X = (\boldsymbol{a} + \boldsymbol{n}_0 \otimes \boldsymbol{n}_0) X = \boldsymbol{a} X + \boldsymbol{n}_0 \otimes (\boldsymbol{n}_0 X),$$

the formulas

$$\langle \operatorname{sym} X, \operatorname{sym} Y \rangle = \langle \operatorname{sym}(\boldsymbol{a}X), \operatorname{sym}(\boldsymbol{a}Y) \rangle + \frac{1}{2} (\boldsymbol{n}_0 X) \cdot (\boldsymbol{n}_0 Y)$$

 $\langle \operatorname{skew} X, \operatorname{skew} Y \rangle = \langle \operatorname{skew}(\boldsymbol{a}X), \operatorname{skew}(\boldsymbol{a}Y) \rangle + \frac{1}{2} (\boldsymbol{n}_0 X) \cdot (\boldsymbol{n}_0 Y)$
 $\operatorname{tr} X = \operatorname{tr}(\boldsymbol{a}X) \quad and \quad \operatorname{tr} Y = \operatorname{tr}(\boldsymbol{a}Y).$

Using these, the densities $W_{\rm mixt}(X,Y)$ and $W_{\rm Coss}(X,Y)$ can be rewritten as [14, Eq. (111)]

$$W_{\mathrm{mixt}}(X,Y) = W_{\mathrm{mixt}}(\boldsymbol{a}X,\boldsymbol{a}Y) + \frac{\mu + \mu_c}{2}(\boldsymbol{n}_0X) \cdot (\boldsymbol{n}_0Y),$$

and

$$W_{\mathrm{Coss}}(X,Y) = W_{\mathrm{mixt}}(\boldsymbol{a}X,\boldsymbol{a}Y) + \frac{2\mu\mu_c}{\mu + \mu_c} (\boldsymbol{n}_0 X) \cdot (\boldsymbol{n}_0 Y),$$

respectively, if X and Y are of the form (12).

Hence, for all relevant arguments the density $W_{\rm Coss}$ differs from $W_{\rm mixt}$ only in the transverse shear coefficient: The geometric mean $\frac{\mu+\mu_c}{2}$ is replaced by the harmonic mean $\frac{2\mu\mu_c}{\mu+\mu_c}$. The same modified membrane energy has been justified by Γ -convergence arguments in [65], and the harmonic mean has already appeared in [60]. We will compare this alternative energy functional numerically to the functional from equation (5) in Chapter 5.2.

2.5. Existence of minimizers. In [34], Ghiba et al. showed existence of minimizers (m, Q_e) for the functional (5) in the space $H^1(\omega, \mathbb{R}^3) \times H^1(\omega, SO(3))$ for the case that ω can be parametrized with a single coordinate chart. However, the result can be easily generalized to shells with a general two-dimensional parameter manifold ω . We briefly state the result here as a preparation for the existence result for geometric finite element solutions in Chapter 4.2. We do not give a detailed proof, because that would largely be a copy of the proof in [34], but Chapter 4.2 on the existence proof for finite element solutions has more details. Note that the result here only covers the case that the Cosserat couple modulus μ_c is strictly positive. Showing existence of solutions for the important case $\mu_c = 0$ requires a different proof, and more regularity of the microrotation field Q_e . Such a proof has appeared in the literature only for the case of a reference surface without curvature [59], but it is clear that that proof could be easily extended to the more general case with curvature as well.

For stating the result in Theorem 18 below we had to change various details, beyond the modifications needed to adapt the statement to our notation. The original result for surfaces with a single coordinate system (Theorem 3.3 in [34]) asked for smoothness of quantities like Q_0 and n_0 , which are not coordinate-independent. As it turns out, though, these smoothness assumptions are not actually needed. We comment on our modified assumptions at the end of this section.

For a rigorous existence result, we need a formal definition of the space of SO(3)-valued Sobolev functions on ω . From the different, non-equivalent definitions in the literature we select the one based on the canonical injection of SO(3) into $\mathbb{R}^{3\times3}$ used also, e.g., in [31, 34] or [68]. With $H^1(\omega, \mathbb{R}^{3\times3})$ the space of $\mathbb{R}^{3\times3}$ -valued first-order Sobolev functions as defined in [78], the corresponding SO(3)-valued Sobolev space is

$$(13) \qquad H^1(\omega,\operatorname{SO}(3)) := \Big\{ R \in H^1(\omega,\mathbb{R}^{3\times 3}) \ : \ R^TR = \mathbbm{1}_3 \text{ and } \det R = 1 \text{ a.e.} \Big\}.$$

We then need appropriate Dirichlet conditions for the shell surface deformation. For this, let γ_d be a subset of ω such that the restriction of H^1 -functions to γ_d is well-defined. This can be a part of the boundary of ω if ω has a boundary, but γ_d can also be an open subset of ω . We prescribe Dirichlet conditions on γ_d by means of a given deformation $\mathbf{m}^* \in H^1(\omega, \mathbb{R}^3)$, and require

(14)
$$\boldsymbol{m} = \boldsymbol{m}^*$$
 on γ_d a.e.

There are several reasonable corresponding conditions for the microrotation field Q_e . The proof in [34] assumes that Q_e is clamped in γ_d , i.e.,

(15)
$$Q_e = Q_e^* \quad \text{on } \gamma_d \quad \text{a.e.},$$

for a given microrotation field $\mathbf{Q}_e^* \in H^1(\omega, \mathrm{SO}(3))$. However, the proof can be easily adapted to the case of Dirichlet conditions for \mathbf{Q}_e on a different set, and it even works with no Dirichlet conditions for \mathbf{Q}_e at all [34, Corollary 3.4].

In the following statement of the existence result, $\kappa_1, \kappa_2 : \omega \to \mathbb{R}$ are the principal curvatures of the reference immersion $\mathbf{m}_0(\omega)$.

Theorem 18 (Existence of minimizers). Assume that the external loads defined in (10) satisfy

$$f \in L^2(\omega, \mathbb{R}^3), \qquad t \in L^2(\gamma_t, \mathbb{R}^3),$$

and that the Dirichlet data satisfies

$$m^* \in H^1(\omega, \mathbb{R}^3), \qquad \mathbf{Q}_e^* \in H^1(\omega, SO(3)).$$

Suppose that the reference shell surface immersion $\mathbf{m}_0 \in H^1(\omega, \mathbb{R}^3)$ is H^2 on each triangle T of T, and such that

$$\nabla \boldsymbol{m}_0 \in L^{\infty}(\omega, \mathbb{R}^{3 \times 2})$$
 and $\sqrt{\det\left((\nabla \boldsymbol{m}_0)^T \nabla \boldsymbol{m}_0\right)} \ge a_0 > 0$ a.e.

in any coordinate system, where a_0 is a constant. Then, for values of the thickness h such that $h|\kappa_1| < \frac{1}{2}$ and $h|\kappa_2| < \frac{1}{2}$, and for constitutive coefficients $\mu > 0$, $\mu_c > 0$, $2\lambda + \mu > 0$, and $b_1, b_2, b_3 > 0$, the functional I defined in (5) has at least one minimizer in the set $H^1(\omega, \mathbb{R}^3) \times H^1(\omega, SO(3))$ subject to the boundary conditions (14) and (possibly) (15).

In [16], Bîrsan and Neff showed existence of solutions under the weaker condition $3\lambda + 2\mu > 0$.

As mentioned above, several technical changes have been made to the statement of Theorem 18 in comparison to Theorem 3.3 of [34]. When reading the following list keep in mind that the map y_0 that is used in [34] corresponds to a representation of \mathbf{m}_0 in local coordinates $\mathbf{m}_0 \circ \tau^{-1} : \mathbb{R}^2 \to \mathbb{R}^3$ in our notation (see also Section 2).

1) The original result required

$$\det(\nabla y_0 \mid \boldsymbol{n}_0) \ge a_0 > 0,$$

instead of

$$\sqrt{\det\left((\nabla \boldsymbol{m}_0)^T \nabla \boldsymbol{m}_0\right)} \ge a_0 > 0,$$

but direct calculations show that the two conditions are the same. The latter form makes it clear that the normal vector n_0 (and hence the local surface orientation) is not involved.

2) For the same reason we write

$$\nabla \boldsymbol{m}_0 \in L^{\infty}(\omega, \mathbb{R}^{3 \times 2})$$

instead of

$$(\nabla y_0 \mid \boldsymbol{n}_0) \in L^{\infty}(\omega, \mathbb{R}^{3\times 3}).$$

These two lines are equivalent, as n_0 is a unit vector field on ω by construction, and therefore in L^{∞} automatically.

- 3) Theorem 3.3 of [34] also demanded that $Q_0 \in H^1(\omega, SO(3))$, but Q_0 is not independent of the choice of local coordinates. A thorough inspection of the proof, though, reveals that this condition is not actually needed.
- 4) Finally, the original proof assumed that the reference shell surface deformation $y_0: \mathbb{R}^2 \to \mathbb{R}^3$ is continuous and injective. However, this is not actually used in the proof, and we have therefore omitted in from Theorem 18.

3. Discretization by geometric finite elements

The discretization of the general geometrically nonlinear Cosserat shell model is special for two reasons. First, the model is based on an abstract parameter surface ω , which cannot be represented directly by an algorithm or data structure. The second, more severe problem is the field of microrotations Q_e . Such a field lives in a non-Euclidean space, and hence it cannot be discretized by standard finite element methods. We instead use geometric finite elements (GFE), which generalize

standard finite elements to non-Euclidean spaces [43]. Sections 3.2 and 3.3 provide a brief introduction, focusing on the relevant case of the target space SO(3).

3.1. Discretizing the shell surface. In the shell model of Chapter 2, the shell surface is represented as an immersion m of an abstract two-dimensional parameter manifold ω into \mathbb{R}^3 . We have already equipped ω with a conforming triangulation \mathcal{T} (Definition 13), which induces a finite collection of homeomorphisms $\{\tau_T\}_{T\in\mathcal{T}}$ from a particular triangle $T_{\text{ref}} \subset \mathbb{R}^2$ (called the reference triangle) to the triangles $T \subset \omega$ of the triangulation. To construct a Lagrange finite element space in this abstract situation let $p \geq 1$ be an approximation order, and choose a global set of corresponding Lagrange points.

Definition 19 (Lagrange points). Let a_1, \ldots, a_N be a finite set of points on ω such that:

(1) For each triangle $T \in \mathcal{T}$, the pulled-back points

$$A_{\mathrm{ref},T} := \left\{ x \in T_{\mathrm{ref}} : \tau_T(x) \in \{a_1, \dots, a_N\} \right\}$$

form a well-posed p-th-order polynomial interpolation problem on $T_{\rm ref}$,

(2) restricting $A_{\text{ref},T}$ to any edge of T_{ref} results in a well-posed p-th-order polynomial interpolation problem on that edge.

Such a set of Lagrange points allows to define Lagrange finite elements on ω mapping into \mathbb{R}^3 . Such finite elements shall be globally continuous on ω , and polynomial on each triangle when expressed in terms of coordinates on T_{ref} . We call the space of such finite elements $S_h(\omega, \mathbb{R}^3)$, and we use it to discretize the shell surface configuration \boldsymbol{m} , and frequently also \boldsymbol{m}_0 .

Conceptually, the two configurations \mathbf{m}_0 and \mathbf{m} are from the same set of objects: they are both immersions from ω into \mathbb{R}^3 . However, while \mathbf{m} is an unknown of the problem, the reference configuration \mathbf{m}_0 forms part of the problem specification. It is used to define the metric and curvature terms $\mathbf{a}, \mathbf{b}, \mathbf{c}, H$ and K, and the area element (4) for the integration of the hyperelastic shell energy density. Therefore, in the actual implementation it is convenient to treat \mathbf{m}_0 as the geometric realization of the finite element grid (cf. the separation of a finite element grid into its topological and geometric aspects in Chapter 5.3 of [66]). That is, from a more algorithmic viewpoint the elements of the finite element grid will be the sets $\mathbf{m}_0(\omega|_T) \subset \mathbb{R}^3$, parametrized via the maps $\mathbf{m}_0 \circ \tau_T : T_{\text{ref}} \to \mathbf{m}_0(\omega|_T), T \in \mathcal{T}$.

To reap the benefits of such an approach, one needs a grid implementation that is able to represent non-affine element geometries, because otherwise all curvature terms appearing in the energy (5) will evaluate to zero. While vanishing curvatures are not a problem per se (the true reference surface to be simulated may be piecewise affine after all), the true power of the shell model comes from the proper handling of the curvature terms.

As both m_0 and m are objects of the same type, it is natural to discretize them in the same way, i.e., to approximate them using finite elements of the same type and order. It is unclear whether this is really necessary, but the experiments in Section 5.1 show a clear influence of the approximation order of m_0 on the simulation result. With a powerful grid data structure such as the one described in [63], it is also possible to approximate m_0 by functions that are more general than piecewise polynomials.

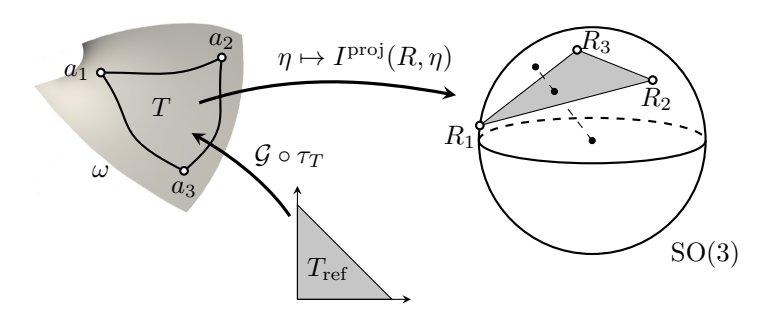


Figure 3. First-order projection-based interpolation

3.2. Geometric interpolation rules. The second major challenge for finite element methods for the Cosserat shell model is how to discretize the field of microrotations Q_e . Such fields cannot be represented by piecewise polynomials, because nontrivial matrix-valued polynomials cannot map into SO(3) everywhere. As a remedy, the Geometric Finite Element method introduces generalized polynomials that do map into SO(3) everywhere, and discretizes manifold-valued functions by piecewise such generalized polynomials. Just as for the regular finite element method, the geometric finite element functions are first defined on the individual grid elements, and are then pieced together via global continuity requirements.

As the function space is nonlinear, the space of finite element functions is not described as the span of a set of basis functions, but rather as the range of an interpolation rule that maps a finite set of values to a function. Several such interpolation rules have been proposed in the literature [43]. We review the two most prominent ones. For what follows let $T \subset \omega$ be a triangle from the triangulation \mathcal{T} of the shell parameter surface ω . This triangle is given a local coordinate system by the map $\tau_T: T_{\text{ref}} \to T$. The interpolation rule will be defined with respect to these coordinates. In a slight abuse of notation, let a_1, \ldots, a_m be the subset of those Lagrange points of Definition 19 contained in T. By construction, there is then a set of scalar p-th-order Lagrangian interpolation functions $\lambda_i: T \to \mathbb{R}$, i.e., polynomials of order p in the local coordinates such that

$$\lambda_i(a_j) = \delta_{ij}$$
 for $i, j = 1, ..., m$, and $\sum_{i=1}^m \lambda_i(\eta) = 1$ $\forall \eta \in T$.

The following constructions now both generalize Lagrangian interpolation of values in $\mathrm{SO}(3)$ given at the Lagrange points.

3.2.1. Projection-based interpolation. The first approach uses an embedding space of SO(3). It was first used for flat, one-dimensional domains in [31, 64], and later generalized to general Riemannian manifolds \mathcal{M} and higher domain dimensions in [37]. Let $\iota: SO(3) \to \mathbb{R}^{3\times 3}$ be the canonical injection, and let $R:=(R_1,\ldots,R_m)\in SO(3)^m$ be a set of values associated to the Lagrange points on T. First we consider the canonical Lagrange interpolation operator $I_{\mathbb{R}^{3\times 3}}$ of values embedded into $\mathbb{R}^{3\times 3}$

$$I_{\mathbb{R}^{3\times3}} : \mathrm{SO(3)}^m \times T \to \mathbb{R}^{3\times3},$$

$$I_{\mathbb{R}^{3\times3}}(R,\eta) \coloneqq \sum_{i=1}^m \iota(R_i) \, \lambda_i(\eta).$$

Even though the R_i are elements of SO(3), the values of $I_{\mathbb{R}^{3\times3}}(R,\cdot)$ will in general not be in SO(3) away from the Lagrange points a_1,\ldots,a_m . To get SO(3)-valued functions we compose $I_{\mathbb{R}^{3\times3}}$ pointwise with the closest-point projection

$$\mathcal{P}: \mathbb{R}^{3\times 3} \to \mathrm{SO}(3), \qquad \mathcal{P}(Q) \coloneqq \underset{P \in \mathrm{SO}(3)}{\arg\min} \|\iota(P) - Q\|,$$

where $\|\cdot\|$ is any unitarily invariant matrix norm. As is well-known, this projection is simply polar(Q), the map onto the orthogonal factor of the polar decomposition [29, 61]. We therefore define SO(3)-valued projection-based interpolation by composition of $I_{\mathbb{R}^{3\times3}}$ and the polar(\cdot) map.

Definition 20 (Projection-based interpolation). Let $T \subset \omega$ be a triangle. Let $\lambda_1, \ldots, \lambda_m$ be a set of p-th-order scalar Lagrangian shape functions on T, and let $R_1, \ldots, R_m \in SO(3)$ be values at the corresponding Lagrange points. We call

$$I^{\text{proj}} : SO(3)^m \times T \to SO(3),$$

$$I^{\operatorname{proj}}(R_1, \dots, R_m; \eta) := \operatorname{polar}\left(\sum_{i=1}^m \iota(R_i) \lambda_i(\eta)\right)$$

p-th-order projection-based interpolation on SO(3).

It is important to realize that there are values R_1, \ldots, R_m for which this construction fails. The polar decomposition is defined for all matrices $X \in \mathbb{R}^{3\times 3}$, but it is unique only if X is invertible. Furthermore, if X is invertible then $\operatorname{polar}(X)$ is in $\operatorname{SO}(3)$ if and only if $\det X > 0$. However, $\det X > 0$ may not hold for all $\eta \in T$ if X is constructed by Lagrange interpolation $X = I_{\mathbb{R}^3 \times 3}(R, \eta)$ in $\mathbb{R}^{3\times 3}$. It is argued in [37, 43] that $\det I_{\mathbb{R}^{3\times 3}}(R, \eta) > 0$ holds for all $\eta \in T$ if the $R_1, \ldots, R_m \in \operatorname{SO}(3)$ are close enough to each other. Such a requirement of locality is common to all geometric finite element constructions in spaces of positive curvature, and hardly ever poses a problem in practical computations. Several efficient algorithms for computing the polar factor of 3×3 matrices are available in the literature [32, 44].

The shell bending–curvature tensor K^e of Definition 8 requires first derivatives of the microrotation field Q_e . Existence of the derivative for projection-based interpolation functions is a consequence of the smoothness of Lagrange interpolation, together with the fact that the closest-point projection onto SO(3) is infinitely differentiable for all invertible matrices [32, 50].

Theorem 21 (Grohs, Hardering, Sander, and Sprecher [37]). Let R_1, \ldots, R_m be coefficients on SO(3) with respect to a p-th-order Lagrange basis $\lambda_1, \ldots, \lambda_m$ on a triangle T. If the function

$$I^{\text{proj}} : SO(3)^m \times T \to SO(3)$$

is defined for particular R_1, \ldots, R_m and η , then it is infinitely differentiable with respect to the R_1, \ldots, R_m and η there.

Computing the derivative of the projection onto SO(3) is discussed, e.g., in [32].

3.2.2. Geodesic interpolation. The second construction works without an embedding space. Recall that the usual Lagrange interpolation of values v_1, \ldots, v_m in \mathbb{R} can be written as a minimization problem

$$\eta \mapsto \underset{w \in \mathbb{R}}{\operatorname{arg\,min}} \sum_{i=1}^{m} \lambda_i(\eta) |v_i - w|^2$$

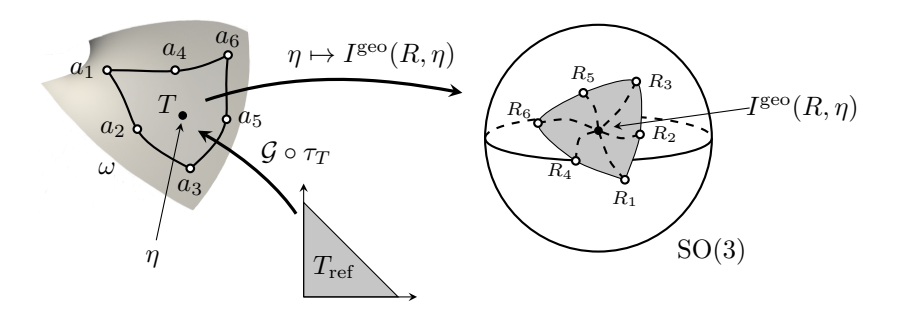


FIGURE 4. Second-order geodesic interpolation

for each $\eta \in T$. This formulation can be generalized to values in SO(3) by replacing the absolute value by the canonical geodesic distance on SO(3) [47]

$$\operatorname{dist}(Q_1, Q_2) := \|\log(Q_1 Q_2^T)\|.$$

Definition 22 (Geodesic interpolation [68]). Let $\lambda_1, \ldots, \lambda_m$ be a set of p-th-order scalar Lagrange functions on T, and let $R_i \in SO(3)$, $i = 1, \ldots, m$, be values at the corresponding Lagrange points. We call

$$I^{\text{geo}} : SO(3)^m \times T \to SO(3)$$

(16)
$$I^{\text{geo}}(R_1, \dots, R_m; \eta) = \underset{R \in SO(3)}{\operatorname{arg min}} \sum_{i=1}^m \lambda_i(\eta) \operatorname{dist}(R_i, R)^2$$

p-th-order geodesic interpolation on SO(3).

Again, this definition is only well-posed if the coefficients R_1, \ldots, R_m are close enough to each other on SO(3). Different proofs for this can be found in [39, 48, 49, 68]. A simple example for first-order geodesic finite elements on triangles is given in [70].

As in the case of projection-based interpolation one can show that the functions created by geodesic interpolation are smooth. This fact follows directly from the implicit function theorem.

Theorem 23 (Sander [68, 69]). Let R_1, \ldots, R_m be coefficients on SO(3) with respect to a p-th-order Lagrange basis $\lambda_1, \ldots, \lambda_m$ on a triangle $T \subset \omega$. If the function

$$I^{\text{geo}} : SO(3)^m \times T \to SO(3)$$

is well-posed in the sense that the minimization Problem (16) defining I^{geo} has a unique solution at R_1, \ldots, R_m and η , then it is infinitely differentiable with respect to the R_i and η .

The papers [68, 69] explain how the derivatives can be computed in practice.

3.2.3. Relationship between geodesic and projection-based interpolation. There is a surprising connection between the geodesic and the projection-based interpolation rule. As observed independently by [31] and [74], we recover the projection-based

interpolation if we replace the geodesic distance in (16) by the Euclidean distance of $\mathbb{R}^{3\times3}$ defined by the Frobenius norm $\|\cdot\|_F$:

(17)
$$\underset{R \in SO(3)}{\operatorname{arg \, min}} \sum_{i=1}^{m} \lambda_{i}(\eta) \|R_{i} - R\|_{F}^{2} = \underset{R \in SO(3)}{\operatorname{arg \, min}} \left(\|R\|_{F}^{2} - 2 \left\langle R, \sum_{i=1}^{m} \lambda_{i}(\eta) R_{i} \right\rangle \right)$$
$$= \underset{R \in SO(3)}{\operatorname{arg \, min}} \left\| R - \sum_{i=1}^{m} \lambda_{i}(\eta) R_{i} \right\|_{F}^{2}$$
$$= \underset{I}{\operatorname{polar}} \left(\sum_{i=1}^{m} \lambda_{i}(\eta) R_{i} \right)$$
$$= I^{\operatorname{proj}}(R_{1}, \dots, R_{m}; \eta).$$

This does not mean, however, that projection-based finite elements are the same as geodesic finite elements. We will use their relationship, however, to prove completeness of projection-based geodesic finite element spaces in Section 4.2.

3.3. Geometric finite element functions. The interpolation functions of the previous section are used to construct generalizations of Lagrange finite element functions with values in SO(3), defined on the triangulated 2-manifold ω .

Just like standard Lagrange finite element spaces, global geometric finite element spaces are constructed by connecting the functions on the individual elements by continuity conditions. By the definition of the global Lagrange point set (Definition 19), such continuity conditions can be fulfilled by the generalized polynomials of the previous section. Let $S_h^{\rm proj}(T)$ and $S_h^{\rm geo}(T)$ be the sets of functions $T\to {\rm SO}(3)$ created by projection-based and geodesic interpolation of a particular polynomial order p, respectively. Then, we define the global spaces (18)

$$S_h^{\mathrm{proj}}(\omega, \mathrm{SO}(3)) := \Big\{ R_h \in C(\omega, \mathrm{SO}(3)) : R_h|_T \in S_h^{\mathrm{proj}}(T, \mathrm{SO}(3)) \quad \forall T \in \mathcal{T} \Big\},$$

and likewise for $S_h^{\text{geo}}(\omega, \text{SO}(3))$. Note that the spaces S_h^{proj} are nested in the sense that low-order spaces are contained in higher-order ones, but the spaces S_h^{geo} are not. Neither of the two families of spaces is nested under uniform grid refinement.

A central feature of the construction of geometric finite elements is their first-order Sobolev conformity. Indeed, recall the definition of the nonlinear function space $H^1(\omega, SO(3))$ from Section 2.5. Then we have the following inclusions:

Lemma 24. Let $S_h^{\text{proj}}(\omega, \text{SO}(3))$ and $S_h^{\text{geo}}(\omega, \text{SO}(3))$ be geometric finite element spaces of order $p \geq 1$. Let $P: A \mapsto \text{polar}(A)$, i.e., the projection from $\mathbb{R}^{3\times 3}$ onto O(3).

i) If the pointwise operator norm of the differential $dP(A): \mathbb{R}^{3\times 3} \to T_{P(A)} \operatorname{SO}(3)$ is globally bounded, then

$$S_h^{\operatorname{proj}}(\omega, \operatorname{SO}(3)) \subset H^1(\omega, \operatorname{SO}(3)).$$

$$ii)$$
 $S_h^{\text{geo}}(\omega, \text{SO}(3)) \subset H^1(\omega, \text{SO}(3)).$

Lemma 24 i) is proved in [37, Sec. 1.1]. Part ii) corresponds to Theorem 3.1 in [69]. The operator norm of the differential $dP(A): \mathbb{R}^{3\times 3} \to T_{P(A)}\operatorname{SO}(3)$ is bounded in each compact subset of the set of invertible real matrices, because, as Kenney and Laub [50] show, we have $\|dP(A)\| = \frac{2}{\sigma_{\min} + \sigma_{\min-1}}$, where σ_{\min} and $\sigma_{\min-1}$ are the two smallest singular values of A.

As a consequence of Lemma 24, discrete approximations $(\boldsymbol{m}_h, \boldsymbol{Q}_{e,h}) \in S_h(\omega, \mathbb{R}^3) \times S_h(\omega, \mathrm{SO}(3))$ are elements of the space $H^1(\omega, \mathbb{R}^3) \times H^1(\omega, \mathrm{SO}(3))$, in which the Cosserat shell problem is well-posed (Theorem 18). (Here we have used $S_h(\omega, \mathrm{SO}(3))$ to denote either $S_h^{\mathrm{proj}}(\omega, \mathrm{SO}(3))$ or $S_h^{\mathrm{geo}}(\omega, \mathrm{SO}(3))$.) This means that the hyperelastic shell energy (5) can be directly evaluated for geometric finite element functions, which facilitates the mathematical understanding of the discrete shell model considerably.

Remark 25. For later reference in Lemma 29 we note that there is also a direct definition of the global geodesic finite element spaces, which incorporates continuity on the level of the scalar Lagrange basis used in Definition 22. Indeed, let $\lambda_1, \ldots, \lambda_N$ now be a global scalar Lagrange finite element basis defined with respect to the global set of Lagrange points a_1, \ldots, a_N of Definition 19. Then it is easily seen that

$$S_h^{\text{geo}}(\omega, \text{SO}(3)) = \left\{ \boldsymbol{R}_h \in L^2(\omega, \mathbb{R}^{3\times 3}) : \exists R_1, \dots, R_N \in \text{SO}(3) \right.$$

$$s.t. \quad \boldsymbol{R}_h(\eta) = \arg\min \sum_{i=1}^N \lambda_i(\eta) \operatorname{dist}(R_i, R)^2 \quad \forall \eta \in \omega \right\}.$$

The minimization problem in this definition looks formally like the one from the original definition (16), but the coefficients and Lagrange basis are now global. Equivalence follows from the fact that for each point η in a triangle $T \subset \omega$ of T, the set of nonzero global Lagrange functions at η is exactly the set of local Lagrange functions used in (16).

Finally, we point out the following equivariance result, which is of central importance for applications in mechanics. It implies that discretizations of frame-indifferent shell models are frame-indifferent as well. The result for S_h^{geo} follows directly from the fact that geodesic interpolation is defined using metric quantities alone, and is hence invariant under isometries [69]. The proof for projection-based finite elements is given in [37].

Lemma 26 (Grohs, Hardering, Sander, and Sprecher [37]). Let O(3) be the orthogonal group on \mathbb{R}^3 , which acts isometrically on SO(3) by left multiplication. Pick any element $Q \in O(3)$. For any geodesic or projection-based finite element function $\mathbf{R}_h \in S_h(\omega, SO(3))$ we define $Q\mathbf{R}_h : \omega \to SO(3)$ by $(Q\mathbf{R}_h)(\eta) = Q(\mathbf{R}_h(\eta))$ for all $\eta \in \omega$. Then $Q\mathbf{R}_h \in S_h(\omega, SO(3))$.

Optimal approximation error bounds for geometric finite element function spaces with values in general Riemannian manifolds \mathcal{M} have been proven in [36, 37, 41, 42]. The same works show optimal discretization error bounds for certain elliptic problems. The application of those abstract results to the energy functionals considered in this paper will be left for future work.

4. Discrete and algebraic Cosserat shell problems

We now apply the geometric finite element method to the Cosserat shell model of Section 2. As the finite element grid we use the triangulation \mathcal{T} of ω (which describes the grid topology) together with the geometry given by the reference immersion m_0 . For each triangle T of \mathcal{T} we then have a mapping from T_{ref} to $m_0(\omega|_T)$ given by $m_0 \circ \tau_T^{-1}$. This is the standard mapping from the reference element to the grid elements used in the finite element method.

Reaping the full power of the shell model requires a finite element grid implementation that supports nonplanar grid elements because otherwise all terms in (5) involving the curvatures K, H, and \boldsymbol{b} of $\boldsymbol{m}_0(\omega)$ would vanish.

4.1. The discrete problem. The hyperelastic shell energy functional I given in (5) is defined on the product of the spaces $H^1(\omega, \mathbb{R}^3)$ and $H^1(\omega, SO(3))$. The first factor is a standard Sobolev space of vector-valued functions on a manifold [78]. For its discretization we use the space $S_h(\omega, \mathbb{R}^3)$ of conforming Lagrange finite elements with values in \mathbb{R}^3 introduced in Section 3.1. We consider Lagrange spaces of any order $p_1 \geq 1$, but omit the order from the notation for simplicity. For the microrotation field $\mathbf{Q}_e : \omega \to SO(3)$ we use either type of geometric finite elements described in the previous chapter. Denote by $S_h(\omega, SO(3))$ the p_2 -th-order geometric finite element space of functions on ω with respect to the grid \mathcal{T} and with values in SO(3). We omit both the order $p_2 \geq 1$ and whether it is a projection-based or geodesic finite element space from the notation.

In the following we write m_h for discrete displacement functions from $S_h(\omega, \mathbb{R}^3)$ and $Q_{e,h}$ for discrete microrotations from $S_h(\omega, SO(3))$. As is widespread in the finite element literature we use a subscript h to denote finite element quantities. This h should not be confused with the thickness parameter that appears in the shell model.

The function spaces may be restricted by Dirichlet conditions. For simplicity we assume that the grid resolves the Dirichlet set γ_d of ω . Let $\boldsymbol{m}_h^* \in S_h(\omega, \mathbb{R}^3)$ be a finite element approximation of the Dirichlet value function $\boldsymbol{m}^* : \omega \to \mathbb{R}^3$ of (14). Then we demand that the discrete displacement \boldsymbol{m}_h fulfills the condition

(19)
$$\boldsymbol{m}_h = \boldsymbol{m}_h^* \quad \text{on } \gamma_d.$$

For the microrotations Q_e we can define discrete approximations of the Dirichlet conditions from Section 2.5. If the continuous model requires to match a Dirichlet value function $Q_e^*: \omega \to SO(3)$ on the set γ_d , then one can select a geometric finite element approximation $Q_{e,h}^* \in S_h(\omega, SO(3))$ of Q_e^* and require

(20)
$$Q_{e,h} = Q_{e,h}^* \quad \text{on } \gamma_d.$$

The case with Dirichlet values on a different part of ω is handled analogously. Also, the existence proof below works if there are no prescribed microrotations at all.

For the formulation of the discrete shell problem we exploit that both projection-based and geodesic approximation spaces $S_h(\omega, \mathrm{SO}(3))$ are contained in H^1 (Lemma 24). Together with the corresponding well-known result for Euclidean finite elements (see, e.g., [17, Satz 5.2]) we can conclude that the Cosserat shell energy functional I is well-defined on the product space $S_h(\omega, \mathbb{R}^3) \times S_h(\omega, \mathrm{SO}(3))$ for all orders $p_1, p_2 \in \mathbb{N}$. A suitable discrete approximation of the Cosserat shell model therefore consists of the unmodified energy functional I restricted to such a space.

Problem 27 (Discrete Cosserat shell problem). Find a pair of functions $(\boldsymbol{m}_h, \boldsymbol{Q}_{e,h})$ with $\boldsymbol{m}_h \in S_h(\omega, \mathbb{R}^3)$ and $\boldsymbol{Q}_{e,h} \in S_h(\omega, \mathrm{SO}(3))$ that minimizes the shell energy functional I given in (5), subject to the constraints (19) (and possibly (20)) on γ_d .

Note that Problem 27 (without the external loads) is frame-indifferent in the sense that

(21)
$$I(R\boldsymbol{m}_h, R\boldsymbol{Q}_{e,h}) = I(\boldsymbol{m}_h, \boldsymbol{Q}_{e,h})$$

for any $m_h \in S_h(\omega, \mathbb{R}^3)$, $\mathbf{Q}_{e,h} \in S_h(\omega, \mathrm{SO}(3))$, and any orthogonal matrix R. Indeed, we have $Rm_h \in S_h(\omega, \mathbb{R}^3)$, and by Lemma 26 we also have $R\mathbf{Q}_{e,h} \in S_h(\omega, \mathrm{SO}(3))$. With this, (21) is simply the frame indifference (9) of the original model.

4.2. Existence of solutions of the discrete problem. In the following, we prove the existence of solutions of the discrete Cosserat shell Problem 27. For this, we show that the energy functional (5) has global minimizers in the discrete product space $S_h(\omega, \mathbb{R}^3) \times S_h(\omega, \text{SO}(3))$ when subject to suitable Dirichlet conditions. Such an existence result is obvious for standard finite element methods, where the finite element space is a finite-dimensional vector subspace of H^1 , and hence closed. The closedness of the nonlinear geometric finite element space $S_h(\omega, \text{SO}(3))$ is less obvious, however, and we show it explicitly in Lemma 29. As in Section 2.5 we only show existence for the Dirichlet condition (20), i.e., the case of $\mathbf{Q}_{e,h}$ being prescribed on γ_d . Solutions also exist without any Dirichlet conditions for the microrotations. The necessary modifications of the proof are discussed in [34].

The existence proof uses the direct method in the calculus of variations. It is a modification of the proof in [34] for existence of minimizers of the continuous model. The crucial fact is that geometric finite element functions are elements of $H^1(\omega, SO(3))$. Therefore, all properties of the energy functional I proved in [34] for the application of the direct method in that space also hold when considering geometric finite element functions. The important new step is to show that weakly H^1 -convergent sequences of such functions have a subsequence that converges to a limit in the geometric finite element space $S_h(\omega, SO(3))$. We will do this in Lemma 29. The following existence theorem is then very similar to its continuous conterpart Theorem 18. Note that the case $\mu_c = 0$ is again not covered—it requires a different proof, and a slight modification of the model.

Theorem 28. Let the external loads satisfy

(22)
$$f \in L^2(\omega, \mathbb{R}^3)$$
 and $t \in L^2(\gamma_t, \mathbb{R}^3)$.

Assume that the reference configuration $\mathbf{m}_0 \in H^1(\omega, \mathbb{R}^3)$ is an immersion that is in H^2 on each triangle, and

$$\nabla \boldsymbol{m}_0 \in L^{\infty}(\omega, \mathbb{R}^{3 \times 2}), \qquad \sqrt{\det\left((\nabla \boldsymbol{m}_0)^T \nabla \boldsymbol{m}_0\right)} \ge a_0 > 0, \ a.e.,$$

where a_0 is a constant. Then, for values of the thickness h such that $h|\kappa_1| < \frac{1}{2}$ and $h|\kappa_2| < \frac{1}{2}$, and for constitutive coefficients such that $\mu > 0$, $\mu_c > 0$, $2\lambda + \mu > 0$, and $b_1, b_2, b_3 > 0$, the minimization problem 27 admits at least one solution in the set $S_h(\omega, \mathbb{R}^3) \times S_h(\omega, SO(3))$, subject to

(23)
$$m_h = m_h^* \quad and \quad Q_{e,h} = Q_{e,h}^* \quad on \, \gamma_d.$$

Proof. As the proof of Theorem 28 is so close to the one of Theorem 3.3 in [34], most of the major steps will only be sketched.

1) In the first step one shows that the functional I of (5) is bounded from below. More formally, one shows that there are constants $c_1 > 0$ and $c_2 \in \mathbb{R}$ such that

(24)
$$I(\boldsymbol{m}_h, \boldsymbol{Q}_{e,h}) \ge c_1 \|\boldsymbol{m}_h - \boldsymbol{m}_h^*\|_{H^1(\omega)}^2 + c_2$$

for all $m_h \in S_h(\omega, \mathbb{R}^3)$ and $Q_{e,h} \in S_h(\omega, SO(3))$. The trick is to see that the internal energy can compensate the unbounded external load functional Π_{ext} of (10).³

2) It then follows that there exists an infimizing sequence $(\boldsymbol{m}_h^k, \boldsymbol{Q}_{e,h}^k)$ in the set \mathcal{A}_h that consists of all functions in $S_h(\omega, \mathbb{R}^3) \times S_h(\omega, SO(3))$ that comply with the Dirichlet conditions (23):

$$\lim_{k\to\infty}I(\boldsymbol{m}_h^k,\boldsymbol{Q}_{e,h}^k)=\inf_{(\boldsymbol{m}_h,\boldsymbol{Q}_{e,h})\in\mathcal{A}_h}I(\boldsymbol{m}_h,\boldsymbol{Q}_{e,h}).$$

Since the boundary value functions m_h^* , $Q_{e,h}^*$ are assumed to be in A_h we can choose the sequence such that

(25)
$$I(\boldsymbol{m}_{h}^{k}, \boldsymbol{Q}_{e,h}^{k}) \leq I(\boldsymbol{m}_{h}^{*}, \boldsymbol{Q}_{e,h}^{*}) < \infty, \quad \forall k \geq 1.$$

3) From (24) and (25) the sequence (\boldsymbol{m}_h^k) is bounded in $H^1(\omega, \mathbb{R}^3)$. Therefore, one can extract a subsequence that converges weakly in $H^1(\omega, \mathbb{R}^3)$, and by Rellich's selection principle this subsequence also converges strongly in $L^2(\omega, \mathbb{R}^3)$.

Let $\widehat{\boldsymbol{m}}_h \in H^1(\omega, \mathbb{R}^3)$ be the limit function. As $S_h(\omega, \mathbb{R}^3)$ is a finite-dimensional vector subspace of $H^1(\omega, \mathbb{R}^3)$ we get $\widehat{\boldsymbol{m}}_h \in S_h(\omega, \mathbb{R}^3)$. Also, $\widehat{\boldsymbol{m}}_h$ complies with the Dirichlet conditions.

4) Likewise, one then shows that there is a $\widehat{Q}_{e,h} \in H^1(\omega, SO(3))$ such that for a subsequence

$$\mathbf{Q}_{e,h}^k \rightharpoonup \widehat{\mathbf{Q}}_{e,h}$$
 in $H^1(\omega, \mathbb{R}^{3\times 3})$

and

$$Q_{e,h}^k \to \widehat{Q}_{e,h}$$
 in $L^2(\omega, \mathbb{R}^{3\times 3})$.

- 5) By [28, Korollar VI.2.7], the L^2 convergence of the subsequence implies that there is a subsubsequence (not relabeled) $(Q_{e,h}^k)$ that converges pointwise a.e. to the same $\widehat{Q}_{e,h} \in H^1(\omega, SO(3))$. Lemma 29 below then shows that the limit is again in $S_h(\omega, SO(3))$, as required.
- 6) To show lower semi-continuity of I, the energy density $W := W_{\text{memb}} + W_{\text{bend}}$ of (6) and (7) is considered as a function of the strains \mathbf{E}^e and \mathbf{K}^e . One shows that the sequences of strains (\mathbf{E}_k^e) and (\mathbf{K}_k^e) corresponding to $(\mathbf{m}_h^k, \mathbf{Q}_{e,h}^k)$ converge weakly in $L^2(\omega, \mathbb{R}^{3\times 3})$ to limit strains $\widehat{\mathbf{E}}^e$, $\widehat{\mathbf{K}}^e$, and that these limits correspond to the limit $(\widehat{\mathbf{m}}_h, \widehat{\mathbf{Q}}_e)$ of $(\mathbf{m}_h^k, \mathbf{Q}_{e,h}^k)$ via the strain formulas of Definition 8.⁴
- 7) The energy density is convex in the strains (albeit nonconvex in ∇m and Q_e), which implies the lower semi-continuity of the internal energy functional

$$\int_{\omega} W(\widehat{\boldsymbol{E}}^{e}, \widehat{\boldsymbol{K}}^{e}) d\omega \leq \liminf_{k \to \infty} \int_{\omega} W(\boldsymbol{E}_{k}^{e}, \boldsymbol{K}_{k}^{e}) d\omega.$$

8) With (22), the L^2 -convergence of \boldsymbol{m}_h^k and $\boldsymbol{Q}_{e,h}^k$, and the continuity of the external load potential we therefore get

$$I(\widehat{\boldsymbol{m}}_h, \widehat{\boldsymbol{Q}}_{e,h}) \leq \liminf_{k \to \infty} I(\boldsymbol{m}_h^k, \boldsymbol{Q}_{e,h}^k).$$

With the standard argument of the direct method one can then conclude that $(\widehat{\boldsymbol{m}}_h, \widehat{\boldsymbol{Q}}_{e,h}) \in S_h(\omega, \mathbb{R}^3) \times S_h(\omega, \mathrm{SO}(3))$ is a minimizing pair.

³This part of the original proof uses the field Q_0 , but can be made independent of it by using the invariance of the matrix norm under orthogonal transformations.

⁴Here again, the original proof in [34] uses the orientation field Q_0 , but the argument can be reformulated without it.

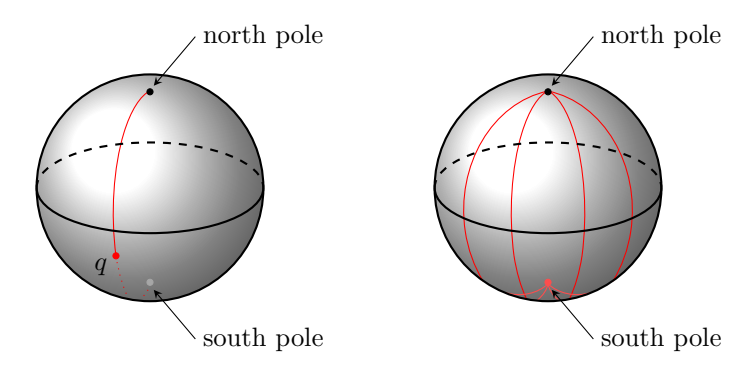


FIGURE 5. The possible non-uniqueness of geodesic interpolation, shown for a first-order geodesic interpolation function from an interval to the sphere. Left: There is a unique such interpolation function from the north pole to any other point q, no matter how close to the south pole. Right: There are infinitely many interpolation functions from the north pole to the south pole.

This existence proof requires in Step 5) that pointwise limits of geometric finite element functions are again geometric finite element functions. This is what we prove next. We prove it for geodesic finite elements only, but by relationship (17) we also obtain the same result for projection-based finite elements. For future reference we temporarily drop the focus on SO(3). Instead, we prove the more general result that the geodesic finite element space $S_h^{\text{geo}}(\omega,(\mathcal{M},d))$ is complete under pointwise convergence for any complete metric space \mathcal{M} with distance $d(\cdot,\cdot)$. This trivially includes the case $\mathcal{M} = \text{SO}(3)$. To streamline the notation we write geodesic finite elements functions without a subscript h in this result.

One apparent difficulty is that limits of uniquely defined geodesic interpolation functions may not be uniquely defined anymore. As an example consider interpolation by a shortest path on the sphere S^2 from the north pole to a point $q \in S^2$. This corresponds to geodesic interpolation on a one-dimensional simplex with two Lagrange points [69, Lemma 2.2]. The interpolation from the north pole by shortest path is uniquely defined for all q not equal to the south pole, and if (q_k) is a sequence of points converging to the south pole, interpolation yields a sequence of unique shortest paths that converge pointwise to a shortest path from the north pole to the south pole (see Figure 5). That limit path is not the only shortest path between the two poles. However, it still satisfies the defining minimization problem (16), and is therefore a geodesic interpolation function in the sense of the definition.

Lemma 29. Let \mathcal{M} be a complete metric space with a metric $d(\cdot, \cdot)$, and let (R_k) be a sequence of geodesic finite element functions with $R_k : \omega \to \mathcal{M}$ for all $k \in \mathbb{N}$, converging pointwise to some limit function $R : \omega \to \mathcal{M}$. Then the limit function is also a geodesic finite element function.

Proof. Let $a_1, \ldots, a_N \in \omega$ be the Lagrange points of Definition 19, and let $\lambda_1, \ldots, \lambda_N$ be the corresponding scalar-valued Lagrange basis. Recalling the global definition in Remark 25 of a geodesic finite element space, we need to show that for any $\eta \in \omega$

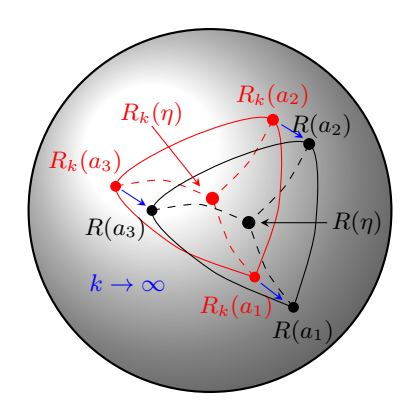


FIGURE 6. The situation in the proof of Lemma 29 for a single triangle, and with first-order interpolation

we have

(26)
$$\sum_{i=1}^{N} \lambda_i(\eta) d(R(\eta), R(a_i))^2 \le \sum_{i=1}^{N} \lambda_i(\eta) d(\hat{R}, R(a_i))^2$$

for any $\hat{R} \in \mathcal{M}$.

For simplicity we omit the η -dependence of the λ_i . Suppose the inequality (26) is false. Then there is an $R^* \in \mathcal{M}$ with

$$\sum_{i=1}^{N} \lambda_i d(R^*, R(a_i))^2 < \sum_{i=1}^{N} \lambda_i d(R(\eta), R(a_i))^2.$$

Let ϵ be a particular fraction of the difference:

$$\epsilon := \frac{1}{3N} \left[\sum_{i=1}^{N} \lambda_i \, d(R(\eta), R(a_i))^2 - \sum_{i=1}^{N} \lambda_i \, d(R^*, R(a_i))^2 \right].$$

We then look at a single addend. If $\lambda_i \geq 0$ we have

$$\lambda_i d(R^*, R_k(a_i))^2 \le \lambda_i \Big[d(R^*, R(a_i)) + d(R(a_i), R_k(a_i)) \Big]^2$$

$$= \lambda_i \Big[d(R^*, R(a_i))^2 + 2 d(R^*, R(a_i)) d(R(a_i), R_k(a_i)) + d(R(a_i), R_k(a_i))^2 \Big].$$

As $R_k(a_i) \to R(a_i)$ we can pick k large enough such that for all i = 1, ..., N we have

$$2\lambda_i d(R^*, R(a_i)) d(R(a_i), R_k(a_i)) + \lambda_i d(R(a_i), R_k(a_i))^2 < \epsilon.$$

If, on the other hand, $\lambda_i < 0$, we bound

$$\lambda_i d(R^*, R_k(a_i))^2 \le \lambda_i \Big[d(R^*, R(a_i)) - d(R(a_i), R_k(a_i)) \Big]^2$$

$$= \lambda_i \Big[d(R^*, R(a_i))^2 - 2d(R^*, R(a_i)) d(R(a_i), R_k(a_i)) + d(R(a_i), R_k(a_i))^2 \Big].$$

Again, for all k large enough we can assume that

$$-2\lambda_i d(R^*, R(a_i)) d(R(a_i), R_k(a_i)) + \lambda_i d(R(a_i), R_k(a_i))^2 < \epsilon.$$

Summing up we get

$$\sum_{i=1}^{N} \lambda_{i} d(R^{*}, R_{k}(a_{i}))^{2} \leq \sum_{i=1}^{N} \lambda_{i} d(R^{*}, R(a_{i}))^{2} + N\epsilon$$

$$< \sum_{i=1}^{N} \lambda_{i} d(R(\eta), R(a_{i}))^{2} - N\epsilon.$$

By continuity of the distance function, we can choose k large enough such that

$$\sum_{i=1}^{N} \lambda_{i} d(R_{k}(\eta), R_{k}(a_{i}))^{2} > \sum_{i=1}^{N} \lambda_{i} d(R(\eta), R(a_{i}))^{2} - \epsilon.$$

Then

$$\sum_{i=1}^{N} \lambda_i d(R^*, R_k(a_i))^2 < \sum_{i=1}^{N} \lambda_i d(R_k(\eta), R_k(a_i))^2.$$

This is a contradiction to the definition of R_k : As it is a geodesic finite element function, $R_k(\eta)$ must be a minimizer of $\sum_{i=1}^N \lambda_i d(\cdot, R_k(a_i))^2$.

4.3. **The algebraic problem.** For the numerical minimization of the Cosserat shell energy we introduce an algebraic formulation. For standard finite elements there is a bijective correspondence between finite element functions and coefficient vectors, via the representations of the functions with respect to a basis. For geometric finite elements this bijection holds only locally. The details are explained, for example, in [68, 70].

Let a_1, \ldots, a_{N_1} be the global set of Lagrange nodes for the p_1 -th order Lagrange finite element space on ω with respect to the triangulation \mathcal{T} . We introduce the evaluation operator

$$\mathcal{E}^{\mathbb{R}^3}: S_h(\omega, \mathbb{R}^3) \to (\mathbb{R}^3)^{N_1}, \qquad \mathcal{E}^{\mathbb{R}^3}(\boldsymbol{m}_h)_i := \boldsymbol{m}_h(a_i), \quad i = 1, \dots, N_1.$$

Similarly, for the global set of nodes a_1, \ldots, a_{N_2} of a Lagrange space of order p_2 we define the evaluation operator

$$\mathcal{E}^{SO(3)}: S_h(\omega, SO(3)) \to SO(3)^{N_2}, \qquad \mathcal{E}^{SO(3)}(\boldsymbol{Q}_{e,h})_i := \boldsymbol{Q}_{e,h}(a_i), \qquad i = 1, \dots, N_2.$$

To construct an algebraic formulation of the shell problem we need the inverse operators $(\mathcal{E}^{\mathbb{R}^3})^{-1}$ and $(\mathcal{E}^{\mathrm{SO}(3)})^{-1}$, which associate functions to sets of values at the Lagrange points. The operator $\mathcal{E}^{\mathbb{R}^3}$ is a bijection and hence $(\mathcal{E}^{\mathbb{R}^3})^{-1}$ is uniquely defined on all of $(\mathbb{R}^3)^{N_1}$. In contrast, $\mathcal{E}^{\mathrm{SO}(3)}$ is not defined for all sets of coefficients from $\mathrm{SO}(3)^{N_2}$, because the interpolation rules of Section 3.2 used to construct finite element functions from coefficients may fail to produce a continuous finite element function, or they may produce more than one from a single set of coefficients. Nevertheless, as shown in [69] the evaluation operator $\mathcal{E}^{\mathrm{SO}(3)}$ is invertible locally under reasonable circumstances, and one can use it to define the algebraic Cosserat shell energy

$$(27) I_{\text{alg}} : D_{\text{alg}} \to \mathbb{R}, I_{\text{alg}}(\overline{\boldsymbol{m}}, \overline{\boldsymbol{Q}}_e) := I((\mathcal{E}^{\mathbb{R}^3})^{-1}(\overline{\boldsymbol{m}}), (\mathcal{E}^{\text{SO}(3)})^{-1}(\overline{\boldsymbol{Q}}_e)),$$

where D_{alg} is a subset of $(\mathbb{R}^3)^{N_1} \times \text{SO}(3)^{N_2}$, and I is the functional (5). The algebraic Cosserat shell problem then is:

Problem 30 (Algebraic Cosserat shell problem). Find a pair $(\overline{m}, \overline{Q}_e) \in D_{\text{alg}}$ that minimizes I_{alg} , subject to suitable Dirichlet conditions.

Problem 30 is a smooth optimization problem in the set D_{alg} , which is an open subset of the manifold $\mathbb{R}^{3N_1} \times \text{SO(3)}^{N_2}$. Such problems can be solved conveniently and efficiently using algorithms for solving optimization problems on manifolds [2]. Details are given in [69, 70].

The algebraic shell minimization problem naturally inherits the frame-indifference property

$$I(R\,\boldsymbol{m}, R\,\boldsymbol{Q}_e) = I(\boldsymbol{m}, \boldsymbol{Q}_e),$$

(where R is any element of SO(3), acting on functions in $H^1(\omega, \mathbb{R}^3)$ and $H^1(\omega, SO(3))$ by pointwise multiplication) of the continuous and discrete formulations.

Theorem 31. When omitting the external loads, the algebraic shell energy functional $I_{\rm alg}$ is frame-indifferent in the sense that

$$I_{\mathrm{alg}}(R\,\overline{\boldsymbol{m}}, R\,\overline{\boldsymbol{Q}}_e) = I_{\mathrm{alg}}(\overline{\boldsymbol{m}}, \overline{\boldsymbol{Q}}_e),$$

for all $R \in SO(3)$, which, by an abuse of notation, now act on the components of $\overline{\boldsymbol{m}} \in (\mathbb{R}^3)^{N_1}$ and $\overline{\boldsymbol{Q}}_e \in SO(3)^{N_2}$.

This important property sets geometric finite element discretizations apart from alternative approaches like [56, 57], which do not preserve the frame indifference of continuous models.

5. Numerical experiments

In this final chapter we demonstrate the capabilities of the shell model and the discretization with a set of numerical experiments. The software for the experiments was implemented in C++, based on the Dune libraries⁵ [9, 66]. The code relies heavily on the ADOL-C algorithmic differentiation library [77] for the computation of first and second derivatives of the energy functional I_{alg} , and on the dune-curvedgrid extension module to the Dune software⁶ [63], which provides finite element grids with nonplanar element geometries. For two-dimensional grids in \mathbb{R}^3 it also provides direct access to the element normal vector \mathbf{n}_0 and to its derivative.

5.1. **Deflection of a half sphere.** In our first numerical example we want to demonstrate that the discretized model does not suffer from shear locking. For the planar Cosserat shell model in [70] we showed experimentally that no shear locking occurs unless the deformation field m is discretized with Lagrange finite elements of first order. A similar result is obtained here, too, but now the approximation order of the reference shell surface $m_0(\omega)$ comes into play as well.

As the problem setting we consider the upper half of a sphere of radius 1 L as the reference configuration $m_0(\omega)$ (the L means length), such that Gauß and mean curvature are $K = 1 L^{-2}$ and $H = 1 L^{-1}$ everywhere, respectively. We clamp the deformation at the equator, but leave the microrotation free of any

⁵https://dune-project.org

 $^{^6 {\}rm https://dune\text{-}project.org/modules/dune\text{-}curvedgrid}$

Dirichlet conditions. We load the shell with a constant vertical tensile volume load of $\mathbf{f} = h \cdot (0,0,10^4)\,\mathrm{M/(LT^2)}$, where M and T mean mass and time, respectively. Note that we scale with the thickness h to represent a load obtained by integrating a three-dimensional volume load over the shell thickness h.

The material parameters are $\lambda = 4.4364 \cdot 10^4 \,\text{M/(LT}^2)$ and $\mu = 2.7191 \cdot 10^4 \,\text{M/(LT}^2)$ for the Lamé parameters, $\mu_c = 0.1\mu$ for the Cosserat couple modulus, $L_c = 5 \cdot 10^{-4} \,\text{L}$ for the internal length, and $b_1 = b_2 = 1$, $b_3 = \frac{1}{3}$. With this choice of b_1 , b_2 , and b_3 , the curvature energy density defined in (8) becomes simply $W_{\text{curv}}(X) = \mu L_c^2 ||X||^2$.

We discretize the deformation functions m_0 and m by Lagrange finite elements, and the microrotation function by geometric finite elements based on geodesic interpolation. For the discrete shell reference geometry $m_{0,h}$ we use elements of first and second order. This means that the element geometries of the finite element grid are either flat triangles or second-order polynomials, constructed such that the triangle corners (and the edge midpoints in the second-order case) lie on the half sphere. Recall that when using flat triangles, all curvature measures in the energy (5) vanish.

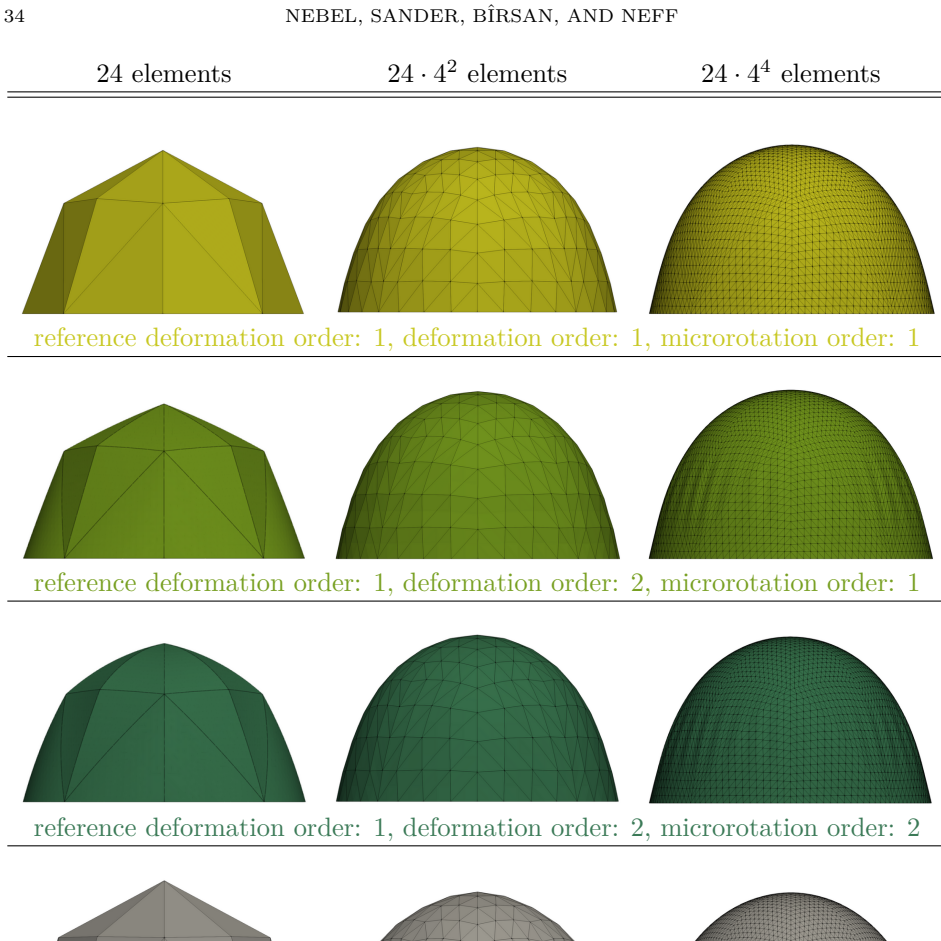
We run simulations for six combinations of approximation orders for the reference deformation m_0 , the deformation m, and the microrotation field Q_e :

scenario	1	2	3	4	5	6	
order: reference deformation $m_{0,h}$	1	1	1	2	2	2	
order: deformation m_h	1	2	2	1	2	2	
order: microrotation $Q_{e,h}$	1	1	2	1	1	2.	

Of the eight possible ways to combine first- and second-order approximations we omit only the cases with first-order deformation and second-order microrotation. The reason is that in the continuous model the third column of the microrotation can be interpreted as an approximation of the normal of $m(\omega)$, which is a first-order derivative of m. Hence, when approximating the deformation by piecewise polynomials of a given order, the exact normal is a piecewise polynomial of one order lower. Consequently, the most natural choice of approximation order is for the deformation to have one order more than the microrotation. In addition, we test the case of equal orders.

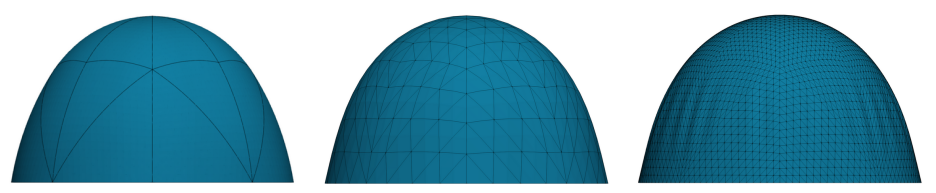
Figure 7 shows qualitative results for a shell thickness of $h=10^{-3}\,\mathrm{L}$ and three different grid resolutions, namely grids with 24 elements, $24\cdot 4^2$ elements, and $24\cdot 4^4$ elements. All six combinations of finite element orders seem to agree on the vertical deflection for the medium and high grid resolutions. With the highly resolved grid, the combinations where the deformation m is approximated with finite element functions of second order show small vertical wrinkles, which can be expected in this load scenario. The simulations with first-order deformations do not show wrinkles.

When looking at the coarse grid results, one can see that the vertical deflection sometimes deviates from the one of the finer grids. To investigate this phenomenon more closely, we measure the deflection of the north pole of the half sphere resulting from the applied load. Figure 8 shows the deflection as a function of the grid resolution. In addition to $h = 10^{-3} \, \text{L}$, the figure shows the same measurements for the thickness values $h = 10^{-4} \, \text{L}$, $h = 10^{-2} \, \text{L}$, and $h = 10^{-1} \, \text{L}$. The behavior is virtually identical for all four thicknesses: The vertical deflection is correctly represented even on the coarser grids if the reference configuration m_0 and the deformation m_0 are both discretized with finite elements of second order. Almost





reference deformation order: 2, deformation order: 1, microrotation order: 1



reference deformation order: 2, deformation order: 2, microrotation order: 1



reference deformation order: 2, deformation order: 2, microrotation order: 2

FIGURE 7. Deflection of a half sphere under vertical tensile load, modelled by a shell with thickness $h = 10^{-3} \, \mathsf{L}$ using different choices of approximation orders for the geometry $m_{0,h}$, for the deformation \boldsymbol{m}_h and for the microrotation $\boldsymbol{Q}_{e,h}$

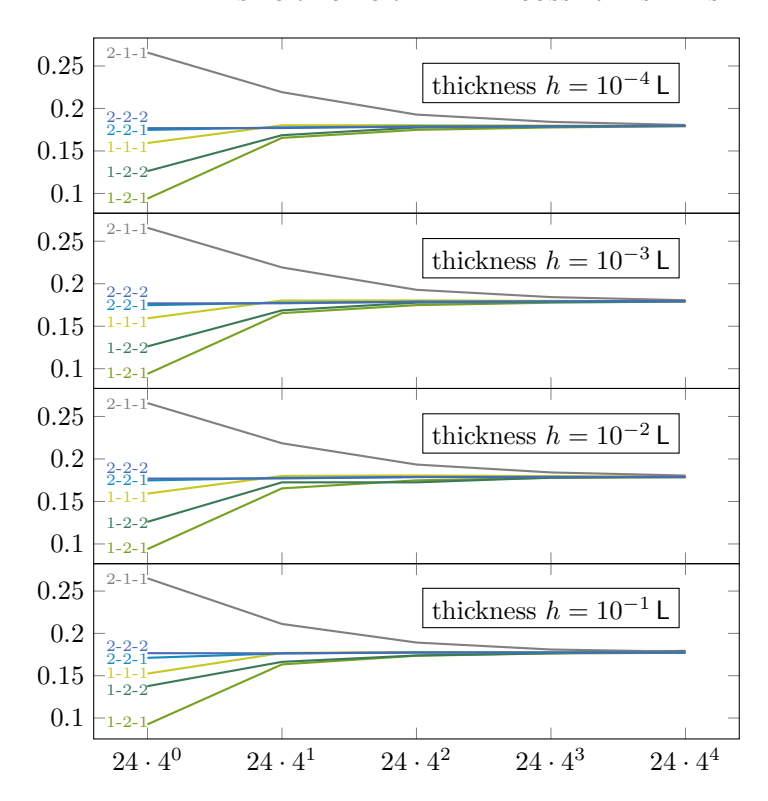


FIGURE 8. Vertical displacement of the north pole as a function of the number of grid elements, for four different thicknesses h and different approximation orders for the element geometry and the finite element functions. The labels of the graphs show: reference deformation order – deformation order – microrotation order.

all other combinations are too stiff if the grid is too coarse, which is the classical locking phenomenon to be expected for badly chosen finite elements.

The one exception is the case with a second-order approximation of the reference geometry together with a first-order approximation of the deformation \boldsymbol{m} , shown in gray. Here, the vertical deflection is too large, and convergence to the correct value for increasing grid resolution is slower than for the locking cases. Note that in this particular situation, the discrete deformation cannot assume the stress-free configuration—a residual pre-stress remains. The exact mechanism of how this pre-stress leads to excessive softness is unclear.

5.2. Comparison with alternative models. Next, we compare the shell model with the related model of Bîrsan [13] briefly described in Remark 17. For the comparison, we use the model problem from the previous section with the same material parameters, i.e., $\lambda = 4.4364 \cdot 10^4 \,\mathrm{M/(LT^2)}$ and $\mu = 2.7191 \cdot 10^4 \,\mathrm{M/(LT^2)}$ for the Lamé parameters, $\mu_c = 0.1\mu$ for the Cosserat couple modulus, $L_c = 5 \cdot 10^{-4} \,\mathrm{L}$ and $b_1 = b_2 = 1$, $b_3 = \frac{1}{3}$. This time we test the model with several different volume loads in the range between $\mathbf{f} = 0.2 \cdot h \cdot (0, 0, 10^4) \,\mathrm{M/(LT^2)}$ and $\mathbf{f} = 1.5 \cdot h \cdot (0, 0, 10^4) \,\mathrm{M/(LT^2)}$. We clamp the deformation m_h at the equator; the microrotation function is not subject to Dirichlet conditions at all. We compare the two models for six thickness

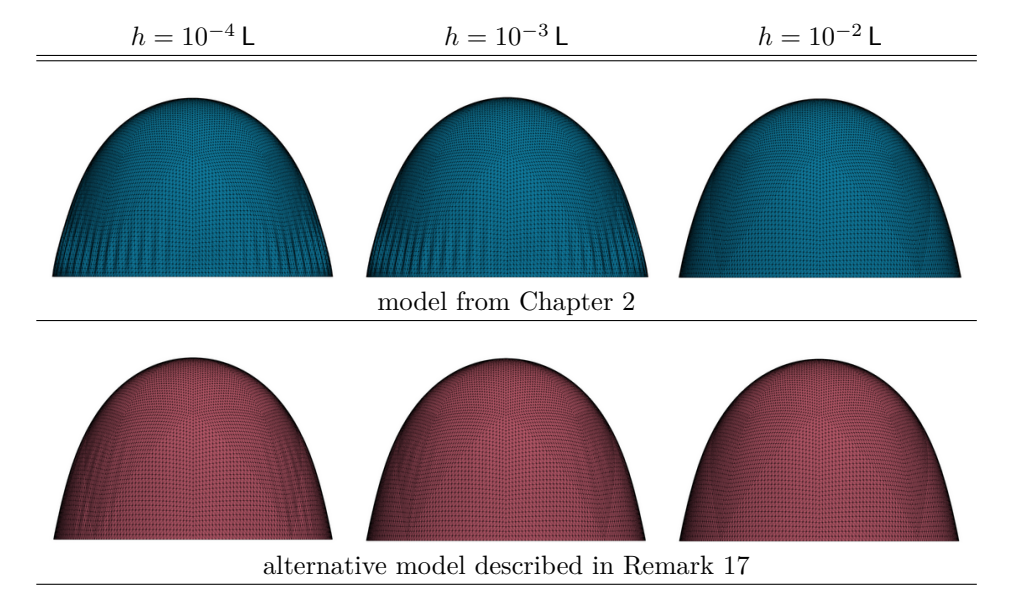


FIGURE 9. Deflection of a half sphere under a vertical tensile load of $\mathbf{f} = 1.5 \cdot h \cdot (0, 0, 10^4) \,\mathrm{M/(LT^2)}$. The pictures show the two Cosserat shell models for different choices of the thickness h.

values between $h=10^{-4}\,\text{L}$ and $h=0.4\,\text{L}$. With the principal curvatures $\kappa_1=\kappa_2=1$ for this example, these thickness values are all below the curvature bounds $h|\kappa_1|<\frac{1}{2}$ and $h|\kappa_2|<\frac{1}{2}$ of Theorem 18.

The reference deformation $m_{0,h}$ and the deformation m_h are represented by Lagrange finite elements of second order and the microrotations are discretized by geodesic finite elements of first order. As shown in the previous section this choice avoids shear locking. We discretize the shell surface ω using a grid consisting of $24 \cdot 4^5$ second-order triangle elements.

Results for $h = 10^{-4} \, \text{L}$, $10^{-3} \, \text{L}$, and $10^{-2} \, \text{L}$, and the load $\mathbf{f} = 1.5 \cdot h \cdot (0, 0, 10^4) \, \text{M/(LT}^2)$ are shown in Figure 9. We see that both models behave similarly. For $h = 10^{-4} \, \text{L}$ and $h = 10^{-3} \, \text{L}$, both models show wrinkles, but the wrinkles are less prominent in the model from [13]. For $h = 10^{-2} \, \text{L}$ neither model shows wrinkles.

For a quantitative comparison we lower the resolution a little, and discretize the shell surface using a grid of only 1580 second-order triangles. Figure 10 shows the vertical displacement of the north pole of the half sphere resulting from four different applied loads as a function of the shell thickness. The force densities are $\mathbf{f} = \alpha \cdot h \cdot (0,0,10^4) \,\mathrm{M/(LT^2)}$ with $\alpha \in \{0.2,0.5,1.0,1.5\}$. One can see that for the weaker loads and the smaller thickness values, the deflections predicted by the two models match almost perfectly. For thicker shells, the model from [13] is slightly softer. For a force density of $\mathbf{f} = 1.5 \cdot h \cdot (0,0,10^4) \,\mathrm{M/(LT^2)}$ there is a noticeable difference between the two model responses. Indeed, while both models show the same qualitative behavior as functions of h, the deflection for the model of Bîrsan [13] is consistently about $0.03 \,\mathrm{L}$ larger than the deflection of the main model for all values of the thickness. Note however that the strains in this case are well beyond

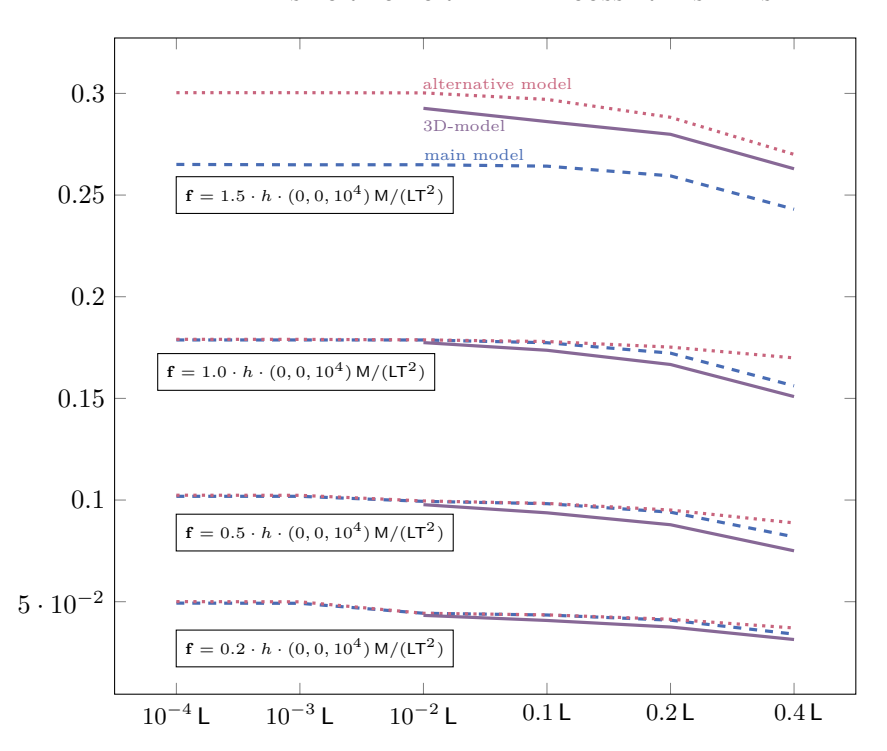


FIGURE 10. Vertical displacement of the half-sphere north pole as a function of the shell thickness for four different volume loads. "Main model" refers to the model introduced in this manuscript (with the factor $\frac{\mu+\mu_c}{2}$ in the transverse shear coefficient), whereas "alternative model" refers to the variant of Bîrsan [13] discussed in Remark 17 (with the factor replaced by $\frac{2\mu\mu_c}{\mu+\mu_c}$). "3D-model" is the three-dimensional Cosserat bulk model of [15] that both shell models are derived from.

the limits of the linear material law used in both shell models, and deviations can therefore be expected.

To assess the behavior of the two shell models even better we also compare with a three-dimensional Cosserat model with linear material response from [15], the parent model that both shell models were derived from. It considers a domain Ω in \mathbb{R}^3 , and deformation and microrotation fields

$$m{m}^{
m 3D}:\Omega
ightarrow\mathbb{R}^3, \qquad m{Q}_e^{
m 3D}:\Omega
ightarrow{
m SO}(3)$$

that minimize

$$(28) \qquad I_{\rm 3D}(\boldsymbol{m}^{\rm 3D},\boldsymbol{Q}_e^{\rm 3D}) := \int_{\Omega} \left[W_{\rm mp}^{\rm 3D}(\overline{\boldsymbol{E}}) + W_{\rm curv}^{\rm 3D}(\boldsymbol{\Gamma}) \right] dV + \text{external loads},$$

where

$$\overline{\boldsymbol{E}} := (\boldsymbol{Q}_e^{\mathrm{3D}})^T \left(\nabla \boldsymbol{m}^{\mathrm{3D}} \right) - \mathbb{1}_3$$

is the non-symmetric strain tensor, and

$$oldsymbol{\Gamma} \coloneqq \operatorname{axl}\left((oldsymbol{Q}_e^{\operatorname{3D}})^T rac{\partial oldsymbol{Q}_e^{\operatorname{3D}}}{\partial x_i}
ight) \otimes oldsymbol{a}^i$$

is the wryness tensor. The vectors a^i are the contravariant basis vectors, of which there are three now. The energy terms are [15, Equation (2.27)]

$$W_{\mathrm{mp}}^{\mathrm{3D}}(\overline{\boldsymbol{E}}) := \mu \|\mathrm{sym}\,\overline{\boldsymbol{E}}\|^2 + \mu_c \|\mathrm{skew}\,\overline{\boldsymbol{E}}\|^2 + \frac{\lambda}{2} (\mathrm{tr}\,\overline{\boldsymbol{E}})^2$$

and [15, Equation (2.30)]

$$W_{\text{curv}}^{\text{3D}}(\mathbf{\Gamma}) := \mu L_c^2(b_1 \|\text{sym}\,\mathbf{\Gamma}\|^2 + b_2 \|\text{skew}\,\mathbf{\Gamma}\|^2 + (b_3 - \frac{b_1}{3})(\text{tr}\,\mathbf{\Gamma})^2).$$

With our choice of parameters b_1 , b_2 , b_3 , the latter again reduces to $W_{\text{curv}}^{\text{3D}}(\Gamma) = \mu L_c^2 ||\Gamma||^2$.

For the three-dimensional domain Ω , we use a half sphere of thickness h, with an outer radius of $1+\frac{h}{2}$ and an inner radius of $1-\frac{h}{2}$. We clamp the deformation $\boldsymbol{m}^{\mathrm{3D}}$ at the equator, and the microrotation function $\boldsymbol{Q}_e^{\mathrm{3D}}$ is again not subject to Dirichlet conditions. The domain is discretized using a three-dimensional unstructured simplex grid constructed such that the element diameters match the mesh size of the two-dimensional grids used for the shells. For the three-dimensional grid we use flat simplex elements, which is justified because the three-dimensional Cosserat energy (28) does not contain terms involving the element geometry curvature. As simulating very thin shells with a bulk model requires either very distorted elements or a very fine grid we do not run the three-dimensional simulations for the thickness values $h = 10^{-4} \, \mathrm{L}$ and $h = 10^{-3} \, \mathrm{L}$.

In comparison to the shell models we see that for the force densities $\mathbf{f} = \alpha \cdot h \cdot (0,0,10^4)\,\mathrm{M/(LT^2)},\ \alpha \in \{0.2,0.5,1.0\}$, the main model approximates the three-dimensional model slightly better. For the thinner shells $(h=0.01\,\mathrm{L})$ and $h=0.1\,\mathrm{L}$, both two-dimensional models match the three-dimensional model almost perfectly. For the force density $\mathbf{f} = 1.5 \cdot h \cdot (0,0,10^4)\,\mathrm{M/(LT^2)}$, the response of the three-dimensional model lies between the shell two models, showing a similar qualitative behavior as a functions of h. The question of whether one of the shell models is better in this regime remains undecided.

5.3. Shells with challenging topology. The next example demonstrates that the shell model and its discretization can handle surfaces with a challenging topology. For this we consider a rectangular block of dimensions $8.5\,\mathrm{L}\times3.5\,\mathrm{L}\times0.5\,\mathrm{L}$, from which material has been removed to leave 24 rotation-symmetric holes. The boundary of the block is a closed two-dimensional surface of genus 24. We use this surface as the reference configuration of a Cosserat shell. The discrete shell model is shown in the top left picture of Figure 11—keep in mind that what looks like a solid three-dimensional object is actually hollow.

For the material behavior we use the same parameters as in the previous examples, i.e., $\lambda = 4.4364 \cdot 10^4 \, \text{M/(LT}^2)$ and $\mu = 2.7191 \cdot 10^4 \, \text{M/(LT}^2)$ for the Lamé parameters, $\mu_c = 0.1 \mu$ for the Cosserat couple modulus, $L_c = 5 \cdot 10^{-4} \, \text{L}$ for the internal length, and $b_1 = b_2 = 1$, $b_3 = \frac{1}{3}$. We choose a shell thickness of $h = 0.05 \, \text{L}$. We discretize the model and its reference configuration m_0 with a grid consisting of 5518 second-order triangle elements. For the deformation m_0 we use second-order Lagrange finite elements, and for the microrotation we use first-order geodesic finite elements.

To drive the model away from the reference configuration we do not apply a volume load. Rather, we clamp the deformation and the microrotation at the left short end and apply a displacement load on the right end. More specifically, we twist the deformation and microrotation of the right end to a rotation of π around the long axis of the object.



FIGURE 11. Deforming the boundary of a rectangular block perforated by 24 holes. The boundary is a closed two-dimensional surface of genus 24. It is displacement-loaded to twist around its long axis. Note that this object is hollow—we are only simulating the boundary.

To reach this state we additionally solve the algebraic minimization Problem 30 at two intermediate load steps at $\frac{\pi}{2}$ and $\frac{3\pi}{4}$, starting always from the solutions of the previous load steps. Figure 11 shows the deformed configurations. One can observe the uniform twisting expected for this type of load. The finite element model seems to handle the large rotations without any difficulties.

5.4. Buckling of a cylinder under a torsion load. With the next example we demonstrate that the model and discretization can represent extreme buckling situations. For this we consider the deformation of a cylinder under a torsion load. Let ω be a topological cylinder, with an immersion m_0 into \mathbb{R}^3 as a cylinder of radius $10\,\text{L}$ and height $15\,\text{L}$, centered around the x_3 -axis. We choose the same material parameters as in the previous examples, i.e., $\lambda = 4.4364 \cdot 10^4\,\text{M/(LT}^2)$ and $\mu = 2.7191 \cdot 10^4\,\text{M/(LT}^2)$ for the Lamé parameters, $\mu_c = 0.1\mu$ for the Cosserat couple modulus, $b_1 = b_2 = 1$, $b_3 = \frac{1}{3}$, and the internal length parameter $L_c = 5 \cdot 10^{-4}\,\text{L}$. The thickness is $h = 0.05\,\text{L}$.

We clamp the cylinder deformation and microrotation at a circular strip of width 3 L at the bottom, and we apply a torsion displacement load at an identical strip at the top of the cylinder. More formally, the Dirichlet set is

$$\gamma_d = \Big\{ \eta \in \omega : (\boldsymbol{m}_0(\eta))_3 \le 3 \text{ or } (\boldsymbol{m}_0(\eta))_3 \ge 12 \Big\},$$

and we apply the torsion load to all points $\eta \in \omega$ with $(m_0(\eta))_3 \geq 12$ by prescribing the microrotation and the x_1 - and x_2 -component of the deformation (but not the x_3 -component). The respective deformation and microrotation functions are

$$m{m}_{lpha}^* = m{m}_{lpha}^{3D} \circ m{m}_0 : \omega o \mathbb{R}^3 \quad ext{and} \quad (m{Q}_e)_{lpha}^* = (m{Q}_e)_{lpha}^{3D} \circ m{m}_0 : \omega o ext{SO}(3)$$

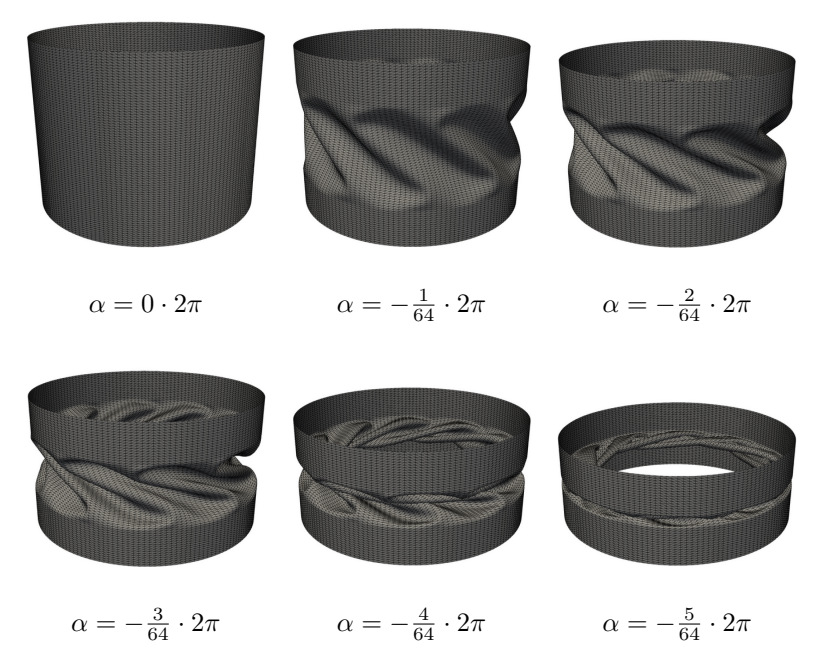


FIGURE 12. Clamped cylinder with torsion displacement loads



FIGURE 13. Paper-made cylinder under a torsion load, from [46]

with

$$m{m}_{lpha}^{3D}(x) = egin{pmatrix} x_1 \ x_2 \ x_3 \end{pmatrix}, \qquad (m{Q}_e)_{lpha}^{3D}(x) = \mathbb{1}_3$$

for all $x \in \mathbb{R}^3$ with $x_3 \leq 3$ and

$$\boldsymbol{m}_{\alpha}^{3D}(x) = \begin{pmatrix} x_1 \cdot \cos \alpha - x_2 \cdot \sin \alpha \\ x_1 \cdot \sin \alpha + x_2 \cdot \cos \alpha \\ \star \end{pmatrix}, \quad (\boldsymbol{Q}_e)_{\alpha}^{3D}(x) = \begin{pmatrix} \cos \alpha & -\sin \alpha & 0 \\ \sin \alpha & \cos \alpha & 0 \\ 0 & 0 & 1 \end{pmatrix}$$

for all $x \in \mathbb{R}^3$ with $x_3 \ge 12$. The functions $\boldsymbol{m}_{\alpha}^*$ and $(\boldsymbol{Q}_e)_{\alpha}^*$ represent a counterclockwise rotation of angle α about the x_3 -axis. The \star denotes that the corresponding deformation component is not prescribed.

We discretize the domain using $80 \times 160 \times 2 = 25600$ triangular elements. For the reference deformation m_0 and the loaded deformation m we use second-order Lagrange finite elements, and we use first-order geodesic finite elements for the microrotation Q_e . Starting from $\alpha = 0$ we load the structure in increments of $-\frac{1}{64} \cdot 2\pi$, up to a load of $\alpha = -\frac{5}{64} \cdot 2\pi$, to obtain a clockwise rotation. The algebraic

minimization problems are solved again starting from the solutions of the previous load steps.

Figure 12 shows the results. The cylinder shows the expected buckling behavior with evenly distributed folds. At the final load the deformable part of the structure is reduced to almost zero height. To highlight the quality of our simulations we compare with a result of Hunt and Ario [46], where a similar torsion problem for a paper-made cylinder has been treated experimentally (Figure 13). In comparison, our simulation shows features very similar to the sharp folds exhibited there. Note, however, that paper deformations are largely isometric, and membrane strains do not occur. A shell model that, unlike ours, does not support membrane deformations could therefore be more appropriate for the modeling of such scenarios.

- 5.5. Non-orientable shell surfaces. In this final section we show simulations of non-orientable shells. It has been argued in Chapter 2 that our shell model is well-defined if ω is non-orientable even though the original derivation in [15, 33] contained terms that are orientation-dependent. We now reconfirm this assertion of Chapter 2 numerically, by testing with two classic examples of non-orientable surfaces, namely the Möbius strip and the Klein bottle.
- 5.5.1. The Möbius strip. A Möbius strip with radius r and width t can be parametrized over the set

$$\omega = \left[-\frac{t}{2}, \frac{t}{2} \right] \times [0, 2\pi],$$

with the following identification of points

$$(u,0) = (-u,2\pi)$$
 $\forall u \in \left[-\frac{t}{2},\frac{t}{2}\right].$

A continuous reference deformation is then

$$m{m}_0:\omega o\mathbb{R}^3, \qquad m{m}_0(u,v) \,=\, egin{pmatrix} \left(r+u\cosrac{v}{2}
ight)\cos v \ \left(r+u\cosrac{v}{2}
ight)\sin v \ u\sinrac{v}{2} \end{pmatrix}.$$

We use the values r = 3 L and t = 4.5 L.

We choose the same material parameters as for the previous examples, i.e., $\lambda = 4.4364 \cdot 10^4 \,\mathrm{M/(LT^2)}$ and $\mu = 2.7191 \cdot 10^4 \,\mathrm{M/(LT^2)}$ for the Lamé parameters, $\mu_c = 0.1\mu$, $L_c = 5 \cdot 10^{-4} \,\mathrm{L}$, and $b_1 = b_2 = 1$, $b_3 = \frac{1}{3}$. The thickness is $h = 0.05 \,\mathrm{L}$. We clamp the deformation and microrotation at all points $\eta \in \omega$ fulfilling $(\boldsymbol{m}_0(\eta))_1 \geq 2.5$, and we load all points fulfilling $(\boldsymbol{m}_0(\eta))_1 \leq -2.5$ with a constant volume force density of $\mathbf{f} = h \cdot (6,0,0) \,\mathrm{M/(LT^2)}$.

The Möbius strip reference deformation is discretized by a uniform grid of $23 \times 120 \times 2 = 5520$ second-order triangles that interpolate \mathbf{m}_0 . We use second-order Lagrange finite elements for the deformation \mathbf{m}_h and second-order geodesic finite elements for the microrotation field $\mathbf{Q}_{e,h}$.

Figure 14 shows the reference deformation with Dirichlet set and volume load on the left, and the deformed configuration in the center. To show how the non-orientability of the surface interacts with the microrotation field Q_e , the right part of Figure 14 shows the discrete microrotation $Q_{e,h}$ for the loaded Möbius strip drawn as an orthonormal frame of director vectors. One sees that they are not in any obvious relationship to the shell surface, in particular the third director is never normal to the surface (and rarely ever close to it). The microrotation $Q_{e,h}$ forms a continuous field on ω even though ω cannot be oriented. This complements



FIGURE 14. Stress-free configuration of the Möbius strip (left), with nodes affected by the volume load (green) and Dirichlet nodes (pink); the deformed configuration of the Möbius strip (center); and the discrete microrotation $Q_{e,h}$ as an orthonormal frame of directors $(d_1 \mid d_2 \mid d_3)$ (right)

the interpretation given in Chapter 2.3: The microrotation Q_e is not the absolute local orientation of the shell, but rather the rotation that moves the reference local orientation Q_0 into the local orientation under load. As such a relative quantity, it is independent of the orientability of the shell surface.

5.5.2. The Klein bottle. A Klein bottle can be constructed using the parameter domain

$$\omega = [0, 2\pi] \times [0, 2\pi]$$

with the identifications

$$(0, v) = (2\pi, v) \quad \forall v \in [0, 2\pi] \quad \text{and} \quad (u, 0) = (2\pi - u, 2\pi) \quad \forall u \in [2, \pi].$$

A suitable reference deformation is then

$$\boldsymbol{m}_{0}(u,v) = \begin{pmatrix} r\left(1-\sin u\right)\,\cos u + \left(2-\cos u\right)\,\cos v\left(2\,e^{-\left(u/2-\pi\right)^{2}}-1\right) \\ \left(2-\cos u\right)\,\sin v \\ t+t\,\sin u + \frac{2-\cos u}{2}\,\sin u\cos v\,e^{-\left(u-3\pi/2\right)^{2}} \end{pmatrix},$$

with r = 1.5 and t = 5. As is well-known, this is not an injective map into \mathbb{R}^3 . However, recall that the global injectivity of the stress-free deformation \mathbf{m}_0 is not required for the shell model (Chapter 2.1). From a mechanical point of view there is no interaction between different intersecting sheets—they slide right through each other.

As previously, we choose the material parameters $\lambda = 4.4364 \cdot 10^4 \,\mathrm{M/(LT^2)}$ and $\mu = 2.7191 \cdot 10^4 \,\mathrm{M/(LT^2)}$ for the Lamé parameters, $\mu_c = 0.1\mu$, $L_c = 5 \cdot 10^{-4} \,\mathrm{L}$ for the internal length, and $b_1 = b_2 = 1$, $b_3 = \frac{1}{3}$. The thickness is $h = 0.05 \,\mathrm{L}$. To eliminate the rigid-body modes we clamp the displacement at all points $\eta \in \omega$ with $(\mathbf{m}_0(\eta))_1 \leq -1.5$. The microrotation is not subject to Dirichlet conditions at all. We then load the Klein bottle using a constant volume force density $\mathbf{f} = h \cdot (10^3, 0, 0) \,\mathrm{M/(LT^2)}$.

We discretize the Klein bottle reference deformation by a structured grid of second-order triangles with $96 \times 128 \times 2 = 24576$ triangles. For the deformation

REFERENCES 43





FIGURE 15. Stress-free configuration of the Klein bottle with Dirichlet nodes marked in purple (left), and deformed configuration under a volume load in the x_1 -direction (right)

m we use second-order Lagrange finite elements, and for the microrotation we use first-order geodesic finite elements.

Figure 15 shows the grid for the reference configuration, and the deformed configuration under load. One can see the folds expected from such a loading scenario, and one can observe that the thin handle does indeed move through the thicker right part without any apparent resistance. Again, the non-orientability of the shell surface does not pose any problem to the shell model and its discretization.

References

- [1] P.-A. Absil, P.-Y. Gousenbourger, P. Striewski, and B. Wirth. "Differentiable piecewise-Bézier surfaces on Riemannian manifolds". In: *SIAM J. Imaging Sci.* 9.4 (2016), pp. 1788–1828. DOI: 10.1137/16M1057978.
- [2] P.-A. Absil, R. Mahony, and R. Sepulchre. Optimization Algorithms on Matrix Manifolds. Princeton University Press, 2008.
- [3] F. Alouges and P. Jaisson. "Convergence of a finite element discretization for the Landau–Lifshitz equations in micromagnetism". In: *Math. Models Methods Appl. Sci.* 16.2 (2006), pp. 299–316.
- [4] P. Areias, T. Rabczuk, and D. Dias-da-Costa. "Assumed-metric spherically interpolated quadrilateral shell element". In: *Finite Elem. Anal. Des.* 66 (2013), pp. 53–67. DOI: 10.1016/j.finel.2012.11.006.
- [5] S. Bartels, K. Böhnlein, C. Palus, and O. Sander. "Benchmarking numerical algorithms for harmonic maps into the sphere". In: arXiv e-prints (2022). arXiv: 2209.13665 [math.NA].
- S. Bartels, B. Kovács, and Z. Wang. "Error analysis for the numerical approximation of the harmonic map heat flow with nodal constraints". In: *arXiv* e-prints (2022). arXiv: 2208.08267 [math.NA].

- [7] S. Bartels, C. Palus, and Z. Wang. "Quasi-optimal error estimates for the approximation of stable harmonic maps". In: *arXiv e-prints* (2022). arXiv: 2209.11985 [math.NA].
- [8] S. Bartels and A. Prohl. "Constraint preserving implicit finite element discretization of harmonic map flow into spheres". In: Math. Comp. 76.260 (2007), pp. 1847–1859.
- [9] P. Bastian, M. Blatt, A. Dedner, N.-A. Dreier, C. Engwer, R. Fritze, C. Gräser, C. Grüninger, D. Kempf, R. Klöfkorn, M. Ohlberger, and O. Sander. "The DUNE framework: Basic concepts and recent developments". In: Computers & Mathematics with Applications 81 (2021), pp. 75–112. DOI: 10.1016/j.camwa. 2020.06.007.
- [10] P. Betsch, A. Menzel, and E. Stein. "On the parametrization of finite rotations in computational mechanics: A classification of concepts with application to smooth shells". In: *Comput. Methods Appl. Mech. Engrg.* 155.3–4 (1998), pp. 273–305. DOI: 10.1016/S0045-7825(97)00158-8.
- [11] P. Betsch and P. Steinmann. "Frame-indifferent beam element based upon the geometrically exact beam theory". In: *Int. J. Num. Meth. Eng.* 54 (2002), pp. 1775–1788. DOI: 10.1002/nme.487.
- [12] K. Bhattacharya, M. Lewicka, and M. Schäffner. "Plates with incompatible prestrain". In: Arch. Rational Mech. Anal. 221 (2016), pp. 143–181. DOI: 10.1007/s00205-015-0958-7.
- [13] M. Bîrsan. "Alternative derivation of the higher-order constitutive model for six-parameter elastic shells". In: Z. Angew. Math. Phys. (ZAMP) 72.50 (2021). DOI: 10.1007/s00033-021-01475-0.
- [14] M. Bîrsan. "Derivation of a refined six-parameter shell model: descent from the three-dimensional Cosserat elasticity using a method of classical shell theory". In: *Math. Mech. Solids* 25(6) (2020), pp. 1318–1339.
- [15] M. Bîrsan, I.-D. Ghiba, R. Martin, and P. Neff. "Refined dimensional reduction for isotropic elastic Cosserat shells with initial curvature". In: Math. Mech. Solids 24 (Sept. 2019), pp. 4000–4019.
- [16] M. Bîrsan and P. Neff. "On the coercivity of strain energy functions in generalized models of 6-parameter shells". In: Sixty Shades of Generalized Continua. Ed. by H. Altenbach, A. Berezovski, F. dell'Isola, and A. Porubov. Advanced Structured Materials. Springer, 2023.
- [17] D. Braess. Finite Elemente. Springer, 2013.
- [18] S. Burzyński, J. Chróścielewski, K. Daszkiewicz, and W. Witkowski. "Geometrically nonlinear FEM analysis of FGM shells based on neutral physical surface approach in 6-parameter shell theory". In: *Composites Part B: Engineering* 107 (2016), pp. 203–213. DOI: 10.1016/j.compositesb.2016.09.015.
- [19] S. Burzyński, J. Chróścielewski, and W. Witkowski. "Geometrically nonlinear FEM analysis of 6-parameter resultant shell theory based on 2-D Cosserat constitutive model". In: *Z. Angew. Math. Mech.* 96 (2016), pp. 191–204. DOI: 10.1002/zamm.201400092.
- [20] J. Chróścielewski, I. Kreja, A. Sabik, and W. Witkowski. "Modeling of composite shells in 6-parameter nonlinear theory with drilling degree of freedom". In: Mech. Adv. Mat. Struct. 18.6 (2011), pp. 403-419. DOI: 10.1080/15376494.2010.524972.

REFERENCES 45

- [21] J. Chróścielewski and W. Witkowski. "FEM analysis of Cosserat plates and shells based on some constitutive relations". In: Z. Angew. Math. Mech. 91 (2011), pp. 400–412. DOI: 10.1002/zamm.201000090.
- [22] M. Crisfield and G. Jelenić. "Objectivity of strain measures in the geometrically exact three-dimensional beam theory and its finite-element implementation". In: Proc. R. Soc. Lond. A 455 (1999), pp. 1125–1147.
- [23] T. tom Dieck. Algebraic Topology. European Mathematical Society, 2008.
- [24] W. Dornisch and S. Klinkel. "Treatment of Reissner-Mindlin shells with kinks without the need for drilling rotation stabilization in an isogeometric framework". In: Comput. Methods Appl. Mech. Engrg. 276 (2014), pp. 35–66.
- [25] W. Dornisch, S. Klinkel, and B. Simeon. "Isogeometric Reissner-Mindlin shell analysis with exactly calculated director vectors". In: Comput. Methods Appl. Mech. Engrg. 253 (2013), pp. 491–504.
- [26] T. X. Duong, F. Roohbakhshan, and R. A. Sauer. "A new rotation-free iso-geometric thin shell formulation and a corresponding continuity constraint for patch boundaries". In: Comput. Methods Appl. Mech. Engrg. 316 (2017), pp. 43–83. DOI: 10.1016/j.cma.2016.04.008.
- [27] E. Efrati, E. Sharon, and R. Kupferman. "Elastic theory of unconstrained non-Euclidean plates". In: *J. Mech. Phys. Solids* 57.4 (2009), pp. 762–775. DOI: 10.1016/j.jmps.2008.12.004.
- [28] J. Elstrodt. Maß- und Integrationstheorie. 7. Edition. Springer, 2011.
- [29] K. Fan and A. J. Hoffman. "Some metric inequalities in the space of matrices". In: *Proc. AMS* 6.1 (1955), pp. 111–116. DOI: 10.2307/2032662.
- [30] A. Fischle and P. Neff. "Grioli's theorem with weights and the relaxed-polar mechanism of optimal Cosserat rotations". In: *Atti Accad. Naz. Lincei Cl. Sci. Fis. Mat. Natur.* 28.3 (2017), pp. 573–600. DOI: 10.4171/RLM/777.
- [31] E. S. Gawlik and M. Leok. "Embedding-based interpolation on the special orthogonal group". In: SIAM J. Sci. Comput. 40.2 (2018), A721–A746. DOI: 10.1137/17M1129416.
- [32] E. S. Gawlik and M. Leok. "Iterative computation of the Fréchet derivative of the polar decomposition". In: *SIAM J. Matrix Anal. Appl.* 38.4 (2017), pp. 1354–1379.
- [33] I.-D. Ghiba, M. Bîrsan, P. Lewintan, and P. Neff. "The isotropic Cosserat shell model including terms up to $O(h^5)$. Part I: Derivation in matrix notation". In: *J. Elast.* 142 (Mar. 2020), pp. 201–262.
- [34] I.-D. Ghiba, M. Bîrsan, P. Lewintan, and P. Neff. "The isotropic Cosserat shell model including terms up to $O(h^5)$. Part II: Existence of mimimizers". In: *J. Elast.* 142 (Mar. 2020), pp. 263–290.
- [35] A. Ghosh, S. Sarkar, L. Nebel, O. Aftenieva, V. Gupta, O. Sander, A. Das, J. Joseph, S. Wießner, T. König, and A. Fery. "Exploring plasmonic resonances toward "large-scale" flexible optical sensors with deformation stability". In: Adv. Functional Mat. (2021). DOI: doi:10.1002/adfm.202101959.
- [36] P. Grohs, H. Hardering, and O. Sander. "Optimal a priori discretization error bounds for geodesic finite elements". In: Found. Comput. Math. 15.6 (2015), pp. 1357–1411. DOI: 10.1007/s10208-014-9230-z.
- [37] P. Grohs, H. Hardering, O. Sander, and M. Sprecher. "Projection-based finite elements for nonlinear function spaces". In: SIAM J. Numer. Anal. 57.1 (2019), pp. 404–428.

- [38] P. Grohs. "Quasi-interpolation in Riemannian manifolds". In: *IMA J. Numer. Anal.* 33.3 (2013), pp. 849–874.
- [39] D. Groisser. "Newton's method, zeroes of vector fields, and the Riemannian center of mass". In: Adv. in Appl. Math. 33.1 (2004), pp. 95–135.
- [40] F. Gruttmann, W. Wagner, L. Meyer, and P. Wriggers. "A nonlinear composite shell element with continuous interlaminar shear stresses". In: *Comp. Mech.* 13 (1993), pp. 175–188.
- [41] H. Hardering. " L^2 -discretization error bounds for maps into Riemannian manifolds". In: $arXiv\ e\text{-}prints\ (2018)$. Extends [42] by several chapters. arXiv: 1612.06086 [math.NA].
- [42] H. Hardering. " L^2 -discretization error bounds for maps into Riemannian manifolds". In: Num. Math. 139.2 (2018), pp. 381–410.
- [43] H. Hardering and O. Sander. "Geometric finite elements". In: *Handbook of Variational Methods for Nonlinear Geometric Data*. Ed. by P. Grohs, M. Holler, and A. Weinmann. Springer, 2020.
- [44] N. J. Higham and V. Noferini. "An algorithm to compute the polar decomposition of a 3 × 3 matrix". In: Numerical Algorithms 73 (2016), pp. 349–369. DOI: 10.1007/s11075-016-0098-7.
- [45] T. J. R. Hughes and W. K. Liu. "Nonlinear finite element analysis of shells: Part I. three-dimensional shells". In: *Comput. Methods Appl. Mech. Engrg.* 26.3 (1981), pp. 331–362. DOI: 10.1016/0045-7825(81)90121-3.
- [46] G. W. Hunt and I. Ario. "Twist buckling and the foldable cylinder: an exercise in origami". In: *Int. J. Non-Linear Mech.* 40 (2005), pp. 833-843. DOI: 10.1016/j.ijnonlinmec.2004.08.011.
- [47] D. Q. Huynh. "Metrics for 3D rotations: Comparison and analysis". In: *J. Math. Imaging Vis.* 35 (2009), pp. 155–165. DOI: 10.1007/s10851-009-0161-2.
- [48] H. Karcher. "Mollifier smoothing and Riemannian center of mass". In: Commun. Pur. Appl. Math. 30 (1977), pp. 509–541.
- [49] W. S. Kendall. "Probability, convexity, and harmonic maps with small image I: uniqueness and fine existence". In: *Proc. London Math. Soc.* s3-61.2 (1990), pp. 371–406.
- [50] C. Kenney and A. J. Laub. "Polar decomposition and matrix sign function condition estimates". In: SIAM J. Sci. Stat. Comput. 12.3 (1991), pp. 488–504. DOI: 10.1137/0912027.
- [51] A. Knapp, L. Nebel, M. Nitschke, O. Sander, and A. Fery. "Controlling line defects in wrinkling: a pathway towards hierarchical wrinkling structures". In: Soft Matter (2021), pp. 5384–5392. DOI: doi:10.1039/D0SM02231D.
- [52] H. Kuo-Mo and C. Yeh-Ren. "Nonlinear analysis of shell structures by degenerated isoparametric shell element". In: Computers & Structures 31.3 (1989), pp. 427–438. DOI: 10.1016/0045-7949(89)90390-8.
- [53] A. Libai and J. G. Simmonds. *The Nonlinear Theory of Elastic Shells*. 2nd edition. Cambridge University Press, 1998. DOI: 10.1017/CB09780511574511.
- [54] J. E. Marsden and T. J. Hughes. Mathematical Foundations of Elasticity. Dover Publications, 1983.
- [55] A. Müller and M. Bischoff. "A consistent finite element formulation of the geometrically non-linear Reissner-Mindlin shell model". In: Arch. Computat. Methods. Eng. (2022). DOI: 10.1007/s11831-021-09702-7.

REFERENCES 47

- [56] W. Müller. "Numerische Analyse und Parallele Simulation von nichtlinearen Cosserat-Modellen". PhD thesis. Karlsruher Institut für Technologie, 2009.
- [57] I. Münch. "Ein geometrisch und materiell nichtlineares Cosserat-model Theorie, Numerik und Anwendungsmöglichkeiten". PhD thesis. Universität Karlsruhe, 2007.
- [58] P. Neff. "A geometrically exact Cosserat-shell model including size effects, avoiding degeneracy in the thin shell limit. Part I: Formal dimensional reduction for elastic plates and existence of minimizers for positive Cosserat couple modulus." In: Continuum Mech. Thermodyn. 16 (2004), pp. 577–628.
- [59] P. Neff. "A geometrically exact planar Cosserat shell-model with microstructure: Existence of minimizers for zero Cosserat couple modulus". In: *Math. Models Methods Appl. Sci.* 17 (2007), pp. 363–392.
- [60] P. Neff and K. Chełmiński. "A geometrically exact Cosserat shell model for defective elastic crystals. Justification via Γ-convergence". In: *Interfaces and Free Boundaries* 9 (2007), pp. 455–492.
- [61] P. Neff, J. Lankeit, and A. Madeo. "On Grioli's minimum property and its relation to Cauchy's polar decomposition". In: *Int. J. Engrg. Sci.* 80 (2014), pp. 209–217. DOI: 10.1016/j.ijengsci.2014.02.026.
- [62] P. M. Pimenta and E. M. B. Campello. "Shell curvature as an initial deformation: a geometrically exact finite element approach". In: *Int. J. Num. Meth. Eng.* 78 (2009), pp. 1094–1112. DOI: 10.1002/nme.2528.
- [63] S. Praetorius and F. Stenger. "Dune-CurvedGrid A Dune module for surface parametrization". In: Arch. Num. Soft. 6.1 (2022). DOI: 10.11588/ans.2022. 1.75917.
- [64] I. Romero. "The interpolation of rotations and its application to finite element models of geometrically exact rods". In: Comp. Mech. 34 (2004), pp. 121–133. DOI: 10.1007/s00466-004-0559-z.
- [65] M. M. Saem, I.-D. Ghiba, and P. Neff. "A geometrically nonlinear Cosserat (micropolar) curvy shell model via Gamma convergence". In: arXiv e-prints (July 2022). to appear in: J. Nonlinear Science. arXiv: 2207.08541 [math.AP].
- [66] O. Sander. DUNE—The Distributed and Unified Numerics Environment. Springer, 2020.
- [67] O. Sander. "Geodesic finite elements for Cosserat rods". In: Int. J. Num. Meth. Eng. 82.13 (2010), pp. 1645–1670.
- [68] O. Sander. "Geodesic finite elements of higher order". In: *IMA J. Numer. Anal.* (2015). DOI: 10.1093/imanum/drv016.
- [69] O. Sander. "Geodesic finite elements on simplicial grids". In: Int. J. Num. Meth. Eng. 92.12 (2012), pp. 999–1025.
- [70] O. Sander, P. Neff, and M. Bîrsan. "Numerical treatment of a geometrically nonlinear planar Cosserat shell model". In: Comp. Mech. 57.5 (2016), pp. 817– 841.
- [71] J. Simo, D. Fox, and M. Rifai. "On a stress resultant geometrically exact shell model. Part III: Computational aspects of the nonlinear theory". In: Comput. Methods Appl. Mech. Engrg. 79.1 (1990), pp. 21–70.
- [72] J. Simo and L. Vu-Quoc. "A three-dimensional finite-strain rod model. Part II: Computational aspects". In: Comput. Methods Appl. Mech. Engrg. 58.1 (1986), pp. 79–116.

- [73] J. Simo and D. Fox. "On a stress resultant geometrically exact shell model. Part I: Formulation and optimal parametrization". In: Comput. Methods Appl. Mech. Engrg. 72.3 (1989), pp. 267–304.
- [74] M. Sprecher. "Numerical methods for optimization and variational problems with manifold-valued data". PhD thesis. ETH Zürich, 2016.
- [75] D. J. Steigmann, M. Bîrsan, and M. Shirani. Lecture Notes on the Theory of Plates and Shells. Springer, 2023. DOI: 10.1007/978-3-031-25674-5.
- [76] W. P. Thurston. Three-Dimensional Geometry and Topology Volume 1. Princeton University Press, 1997.
- [77] A. Walther and A. Griewank. "Getting started with ADOL-C". In: *Combinato-rial Scientific Computing*. Ed. by U. Naumann and O. Schenk. Chapman-Hall CRC Computational Science, 2012, pp. 181–202.
- [78] J. T. Wloka. Partial Differential Equations. Cambridge University Press, 1987.
- [79] P. Wriggers and F. Gruttmann. "Thin shells with finite rotations formulated in Biot stresses: theory and finite element formulation". In: *Int. J. Num. Meth. Eng.* 36 (1993), pp. 2049–2071.

LISA JULIA NEBEL, TECHNISCHE UNIVERSITÄT DRESDEN, INSTITUT FÜR NUMERISCHE MATHE-MATIK, ZELLESCHER WEG 12-14, 01069 DRESDEN, GERMANY, ◎ 0000-0002-7200-0312 Email address: lisa_julia.nebel@tu-dresden.de

OLIVER SANDER, TECHNISCHE UNIVERSITÄT DRESDEN, INSTITUT FÜR NUMERISCHE MATHEMATIK, ZELLESCHER WEG 12–14, 01069 DRESDEN, GERMANY, © 0000-0003-1093-6374 Email address: oliver.sander@tu-dresden.de

Mircea Bîrsan, Universität Duisburg–Essen, Lehrstuhl für Nichtlineare Analysis und Modellierung, Fakultät für Mathematik, Thea-Leymann Str. 9, 45127 Essen, Germany, and Department of Mathematics, University "A.I. Cuza" of Iaşı, 700506 Iaşı, Romania, 0000-0002-1360-4044

Email address: mircea.birsan@uni-due.de

Patrizio Neff, Universität Duisburg–Essen, Lehrstuhl für Nichtlineare Analysis und Modellierung, Fakultät für Mathematik, Thea-Leymann Str. 9, 45127 Essen, Germany, 0000-0002-1615-8879

Email address: patrizio.neff@uni-due.de